

THE BUZZARD FLOCK: DARK ENERGY SURVEY SYNTHETIC SKY CATALOGS

J. DEROSE,^{1,2,3} R. H. WECHSLER,^{1,2,3} M. R. BECKER,⁴ M. T. BUSH,⁵ E. S. RYKOFF,^{2,3} N. MACCRANN,^{6,7} B. ERICKSON,⁸
A. E. EVRARD,^{9,8} A. KRAVTSOV,¹⁰ D. GRUEN,^{1,2,3} S. ALLAM,¹¹ S. AVILA,¹² S. L. BRIDLE,¹³ D. BROOKS,¹⁴ E. BUCKLEY-GEER,¹¹
A. CARNERO ROSELL,^{15,16} M. CARRASCO KIND,^{17,18} J. CARRETERO,¹⁹ F. J. CASTANDER,^{20,21} R. CAWTHON,²² M. CROCCE,^{20,21}
L. N. DA COSTA,^{16,23} C. DAVIS,² J. DE VICENTE,¹⁵ J. P. DIETRICH,^{24,25} P. DOEL,¹⁴ A. DRLICA-WAGNER,^{11,10} P. FOSALBA,^{20,21}
J. FRIEMAN,^{11,10} J. GARCÍA-BELLIDO,²⁶ G. GUTIERREZ,¹¹ W. G. HARTLEY,^{14,27} D. L. HOLLOWOOD,²⁸ B. HOYLE,^{29,30}
D. J. JAMES,³¹ E. KRAUSE,³² K. KUEHN,³³ N. KUROPATKIN,¹¹ M. LIMA,^{34,16} M. A. G. MAIA,^{16,23} F. MENANTEAU,^{17,18}
C. J. MILLER,^{9,8} R. MIQUEL,^{35,19} R. L. C. OGANDO,^{16,23} A. A. PLAZAS,³⁶ A. K. ROMER,³⁷ E. SANCHEZ,¹⁵ R. SCHINDLER,³
S. SERRANO,^{20,21} I. SEVILLA-NOARBE,¹⁵ M. SMITH,³⁸ E. SUCHYTA,³⁹ M. E. C. SWANSON,¹⁸ G. TARLE,⁸ AND V. VIKRAM⁴
(DES COLLABORATION)

¹Department of Physics, Stanford University, 382 Via Pueblo Mall, Stanford, CA 94305, USA

²Kavli Institute for Particle Astrophysics & Cosmology, P. O. Box 2450, Stanford University, Stanford, CA 94305, USA

³SLAC National Accelerator Laboratory, Menlo Park, CA 94025, USA

⁴Argonne National Laboratory, 9700 South Cass Avenue, Lemont, IL 60439, USA

⁵Securiti, mbusha@gmail.com

⁶Center for Cosmology and Astro-Particle Physics, The Ohio State University, Columbus, OH 43210, USA

⁷Department of Physics, The Ohio State University, Columbus, OH 43210, USA

⁸Department of Physics, University of Michigan, Ann Arbor, MI 48109, USA

⁹Department of Astronomy, University of Michigan, Ann Arbor, MI 48109, USA

¹⁰Kavli Institute for Cosmological Physics, University of Chicago, Chicago, IL 60637, USA

¹¹Fermi National Accelerator Laboratory, P. O. Box 500, Batavia, IL 60510, USA

¹²Institute of Cosmology and Gravitation, University of Portsmouth, Portsmouth, PO1 3FX, UK

¹³Jodrell Bank Center for Astrophysics, School of Physics and Astronomy, University of Manchester, Oxford Road, Manchester, M13 9PL, UK

¹⁴Department of Physics & Astronomy, University College London, Gower Street, London, WC1E 6BT, UK

¹⁵Centro de Investigaciones Energéticas, Medioambientales y Tecnológicas (CIEMAT), Madrid, Spain

¹⁶Laboratório Interinstitucional de e-Astronomia - LIneA, Rua Gal. José Cristino 77, Rio de Janeiro, RJ - 20921-400, Brazil

¹⁷Department of Astronomy, University of Illinois at Urbana-Champaign, 1002 W. Green Street, Urbana, IL 61801, USA

¹⁸National Center for Supercomputing Applications, 1205 West Clark St., Urbana, IL 61801, USA

¹⁹Institut de Física d'Altes Energies (IFAE), The Barcelona Institute of Science and Technology, Campus UAB, 08193 Bellaterra (Barcelona) Spain

²⁰Institut d'Estudis Espacials de Catalunya (IEEC), 08034 Barcelona, Spain

²¹Institute of Space Sciences (ICE, CSIC), Campus UAB, Carrer de Can Magrans, s/n, 08193 Barcelona, Spain

²²Physics Department, 2320 Chamberlin Hall, University of Wisconsin-Madison, 1150 University Avenue Madison, WI 53706-1390

²³Observatório Nacional, Rua Gal. José Cristino 77, Rio de Janeiro, RJ - 20921-400, Brazil

²⁴Excellence Cluster Universe, Boltzmannstr. 2, 85748 Garching, Germany

²⁵Faculty of Physics, Ludwig-Maximilians-Universität, Scheinerstr. 1, 81679 Munich, Germany

²⁶Instituto de Física Teórica UAM/CSIC, Universidad Autónoma de Madrid, 28049 Madrid, Spain

²⁷Department of Physics, ETH Zurich, Wolfgang-Pauli-Strasse 16, CH-8093 Zurich, Switzerland

²⁸Santa Cruz Institute for Particle Physics, Santa Cruz, CA 95064, USA

²⁹Max Planck Institute for Extraterrestrial Physics, Giessenbachstrasse, 85748 Garching, Germany

³⁰Universitäts-Sternwarte, Fakultät für Physik, Ludwig-Maximilians Universität München, Scheinerstr. 1, 81679 München, Germany

³¹Harvard-Smithsonian Center for Astrophysics, Cambridge, MA 02138, USA

³²Department of Astronomy/Steward Observatory, 933 North Cherry Avenue, Tucson, AZ 85721-0065, USA

³³Australian Astronomical Optics, Macquarie University, North Ryde, NSW 2113, Australia

³⁴Departamento de Física Matemática, Instituto de Física, Universidade de São Paulo, CP 66318, São Paulo, SP, 05314-970, Brazil

³⁵Institució Catalana de Recerca i Estudis Avançats, E-08010 Barcelona, Spain

³⁶Jet Propulsion Laboratory, California Institute of Technology, 4800 Oak Grove Dr., Pasadena, CA 91109, USA

³⁷Department of Physics and Astronomy, Pevensey Building, University of Sussex, Brighton, BN1 9QH, UK

³⁸School of Physics and Astronomy, University of Southampton, Southampton, SO17 1BJ, UK

³⁹Computer Science and Mathematics Division, Oak Ridge National Laboratory, Oak Ridge, TN 37831

ABSTRACT

We present a suite of 18 synthetic sky catalogs designed to support science analysis of galaxies in the Dark Energy Survey Year 1 (DES Y1) data. For each catalog, we use a computationally efficient empirical approach, ADDGALS, to embed galaxies within light-cone outputs of three dark matter simulations that resolve halos with masses above $\sim 5 \times 10^{12} h^{-1} M_{\odot}$ at $z \leq 0.32$ and $10^{13} h^{-1} M_{\odot}$ at $z \sim 2$. The embedding method is tuned to match the observed evolution of galaxy counts at different luminosities as well as the spatial clustering of the galaxy population. Galaxies are lensed by matter along the line of sight — including magnification, shear, and multiple images — using CALCLENS, an algorithm that calculates shear with 0.42 arcmin resolution at galaxy positions in the full catalog. The catalogs presented here, each with the same Λ CDM cosmology (denoted Buzzard), contain on average 820 million galaxies over an area of 1120 square degrees with positions, magnitudes, shapes, photometric errors, and photometric redshift estimates. We show that the weak-lensing shear catalog, REDMAGIC galaxy catalogs and REDMAPPER cluster catalogs provide plausible realizations of the same catalogs in the DES Y1 data by comparing their magnitude, color and redshift distributions, angular clustering, and mass-observable relations, making them useful for testing analyses that use these samples. We make public the galaxy samples appropriate for the DES Y1 data, as well as the data vectors used for cosmology analyses on these simulations.

1. INTRODUCTION

The laboratory provided to us by the night sky has enabled great advances in our understanding of the universe and the laws that govern it. In particular, astronomical observations currently provide the only evidence for the existence of dark matter and dark energy (Zwicky 1933; Rubin et al. 1980; Planck Collaboration et al. 2018; Perlmutter et al. 1999; Riess et al. 1998), and may provide one of the only avenues for studying energies near the Planck scale in the foreseeable future by measuring observable signals related to cosmic inflation (e.g. Arkani-Hamed & Maldacena 2015; Abazajian et al. 2016). In the near future, ongoing and next generation galaxy surveys will measure tens of millions of spectra and image tens of billions of galaxies in order to precisely constrain the properties of dark matter, dark energy, neutrinos and inflation. These surveys include the Dark Energy Survey (DES)¹, Kilo-Degree Survey (KiDS)², Hyper Suprime Cam (HSC)³, Dark Energy Spectroscopic Instrument (DESI)⁴, Prime Focus Spectrograph (PFS)⁵, Large Synoptic Survey Telescope (LSST)⁶, Euclid⁷ and the Wide Field InfraRed Survey Telescope (WFIRST)⁸.

Succeeding in this endeavor will require systematics associated with cosmological observables, astrophysical, theoretical and observational, to be controlled at an exquisite level. Further, with many cosmological probes computed from the same data, the characterization of common sources of systematic error is a crucial priority.

A primary avenue for understanding systematic errors will be through the analysis of synthetic or “mock” catalogs. These catalogs attempt to simulate, at varying levels of fidelity, the full range of physical processes that influence various observables in large-area sky surveys, including galaxy fluxes, sizes, and shapes. Such synthetic catalogs are not designed to calibrate the tools used in actual survey analysis. Rather, they provide a development environment that supports quantitative investigation of sources of systematic error in specific, model-dependent scenarios. Fundamentally, these catalogs are *plausible* rather than *definitive* expectations for a given cosmology.

Ideally, these synthetic catalogs would be constructed using methods able to predict the intrinsic distribution and properties of galaxies via *ab initio* solutions of coupled dark matter and baryonic evolution (e.g. Evrard 1988). Progress is

being made on this front, both in running large lower resolution simulations (Schaye et al. 2015; Springel et al. 2018; Naiman et al. 2018; Marinacci et al. 2018; Nelson et al. 2018; Pillepich et al. 2018), and more detailed high resolution zoom-in simulations (Kim et al. 2014; Hopkins et al. 2018), but it will be many years before these approaches can simulate the volumes being observed by wide-field galaxy surveys at the necessary resolution while reproducing observed galaxy populations with as good of fidelity as empirical models.

In the interim, a more practical alternative that has had success is to place modeled galaxies in their associated dark matter structures using an empirical or phenomenological model such as subhalo abundance matching related methods (Tasitsiomi et al. 2004; Conroy et al. 2006a; Hearin & Watson 2013; Crocce et al. 2015; Moster et al. 2018; Behroozi et al. 2018) or halo occupation distribution (HOD) models (Jing 1998; Seljak 2000; Yang et al. 2003; Berlind & Weinberg 2002; Zheng et al. 2005; Mandelbaum et al. 2006; van den Bosch et al. 2007; Zehavi et al. 2011; Carretero et al. 2015; Zu & Mandelbaum 2015). The best of these empirical approaches are able to precisely reproduce luminosity functions, star formation histories, and observed luminosity and color dependent clustering of galaxies, something which no other model of galaxy formation can achieve (Moster et al. 2018; Behroozi et al. 2018). Semi analytic models (SAMs) (White & Frenk 1991; Kauffmann et al. 1993; Somerville & Primack 1999; Cole et al. 2000; Bower et al. 2006; Guo et al. 2013; Benson et al. 2002) attempt to include more physics than the empirical models mentioned above and so in principle are more predictive, but in doing so they have struggled to reproduce some of the observables to the same level of fidelity as empirical models. These various approaches to modeling the galaxy–halo connection have recently been reviewed by Wechsler & Tinker (2018).

In this work, we present a suite of synthetic catalogs for the Dark Energy Survey (DES) constructed using a model tuned to match the properties of sub-halo abundance matching (SHAM), and compare our results to the first year of DES data (DES Y1). Our methodology, while currently tuned to the DES, is applicable generically to a variety of large-area photometric and spectroscopic surveys. Instead of employing a single, large N-body simulation, we take a lightweight approach involving sets of smaller dark matter-only simulations that are readily generated on teraflop computing platforms. We then apply the ADDGALS algorithm, described in detail in the companion to this work, Wechsler et al. (2019), to populate these dark matter simulations with galaxies. Post-processing routines, including ray-tracing to compute weak-lensing, add a number of physical and instrumental effects, which cause properties of the observed galaxy population to deviate from their intrinsic values. Fig. 1 shows an exam-

¹ <https://www.darkenergysurvey.org>

² <http://kids.strw.leidenuniv.nl>

³ <http://www.subarutelescope.org/Projects/HSC>

⁴ <https://www.desi.lbl.gov/>

⁵ <https://pfs.ipmu.jp/>

⁶ <http://www.lsst.org>

⁷ <http://http://sci.esa.int/euclid/>

⁸ <http://wfirst.gsfc.nasa.gov>

ple of one of our simulations, displaying the underlying projected dark matter distribution, an observed optical cluster catalog, and weak-lensing shear around a massive halo.

In principle, ADDGALS can be used on even lower resolution simulations than the ones presented here, including those produced by approximate N -body methods such as COLA (Tassev et al. 2013; Izard et al. 2018). The main requirement on the resolution of the simulations used by ADDGALS is that halos above $\sim 10^{13}h^{-1}M_{\odot}$ be resolved well, driven by the need to resolve the halos hosting galaxy cluster populations. Modern approximate N -body codes are capable of reproducing the correct number densities and large-scale clustering of these objects, but the small-scale density profiles of halos suffer from resolution effects. As such, the use case for approximate N -body simulations is restricted to applications which do not sensitively depend on small scale galaxy or matter density profiles. As one of the goals of the simulations presented here is to reproduce all of the galaxy-based cosmological observables in DES, including the abundances of optically selected clusters as a function of cluster richness, a quantity that depends sensitively on galaxy profiles in halos, we have forgone using approximate N -body simulations, opting instead for traditional N -body simulations with modest resolution.

The work presented here is most similar in approach to the MICE simulation (Fosalba et al. 2015a; Crocce et al. 2015; Fosalba et al. 2015b), with the main qualitative differences being that our methodology allows for the use of lower resolution simulations, and that we include full ray-tracing rather than using the Born approximation to compute weak-lensing observables. Simulations more focused on weak-lensing statistics using full ray-tracing have also recently been released (Takahashi et al. 2017; Harnois-Déraps et al. 2018).

The catalogs we present here are particularly useful because they can be used to study many large-scale structure probes simultaneously, including galaxy clustering, optically selected galaxy clusters, weak-lensing shear correlation functions, and the lensing profiles of galaxies and clusters. Further, the total computing time for both the numerical simulations and the post-processing steps is approximately 150K CPU hours per 10,313 square degrees of unique, contiguous sky. This modest scale has allowed us to produce multiple such sky surveys already, and will allow for the production of many more in the near future to meet the needs of DES analyses. Multiple realizations are essential for testing the statistical performance of cosmological analyses and studying the covariances of cosmological observables.

Indeed, earlier versions of the catalogs presented here have already been essential for a variety of purposes: development of the DES data management pipeline, testing and improvement of galaxy cluster finders, (Miller et al. 2005; Koester

et al. 2007b; Dong et al. 2008; Hao et al. 2010; Soares-Santos et al. 2011), development of methods to measure cosmological parameters from galaxy clusters (Koester et al. 2007a; Johnston et al. 2007; Rozo et al. 2007a,b; Becker et al. 2007; Sheldon et al. 2009; Hansen et al. 2009; Tinker et al. 2011), development and testing of photometric redshift algorithms (Gerdes et al. 2010; Cunha et al. 2012, 2014; Bonnett et al. 2016; Leistedt et al. 2016; Hoyle et al. 2018; Gatti et al. 2018), development of various approaches using galaxy shear (Becker et al. 2016; Troxel et al. 2018; Chang et al. 2018), and in testing the robustness of DES Y1 cosmology pipelines (DES Collaboration et al. 2017; Krause et al. 2017; MacCrann et al. 2018; Friedrich et al. 2018; Gruen et al. 2018).

This work serves as an explication of the general methodology behind the production of these simulations, pieces of which have been progressively improved over the past decade. While the methodology behind these simulations is still under active development, the versions of the simulations presented here represent the current state of our modeling capabilities. In order to assure the usability of simulations for various analyses, it is vital that working groups familiar with the needs of individual analyses contribute quality assurance (QA) requirements that simulations must meet. Such an exercise was pursued on a qualitative basis in the construction of the catalogs presented here, and so the comparisons to data presented in this work will not be accompanied by quantitative pass/fail verdicts. Instead we will emphasize where these catalogs have found most use within DES, and caution the reader about aspects that are particularly untrustworthy. A much more rigorous QA exercise is being pursued within the LSST Dark Energy Science Collaboration (LSST DESC), and the authors are actively engaged in that work (Mao et al. 2018).

We begin in §2 by describing the observables that we wish to simulate. In §3 we give a brief summary of the algorithms we applied to produce each synthetic catalog. Note that for clarity, we present the majority of the technical details in the appendices, and in a companion paper describing the implementation and performance of ADDGALS in detail (Wechsler et al. 2019). In §4, we describe our simulated weak-lensing source and lens samples and a photometrically selected cluster sample, comparing them to their analogs in the DES Y1 data. In §5 we summarize and discuss the areas that are most in need of further investigation. Throughout this manuscript, we quote magnitudes using the AB system and $h = 1.0$ units.

2. SIMULATION REQUIREMENTS

The simulations presented in this work are intended to model observables that are used in a range of DES analyses, but, in practice, the analyses that place the most stringent requirements on simulation fidelity are the key cosmology

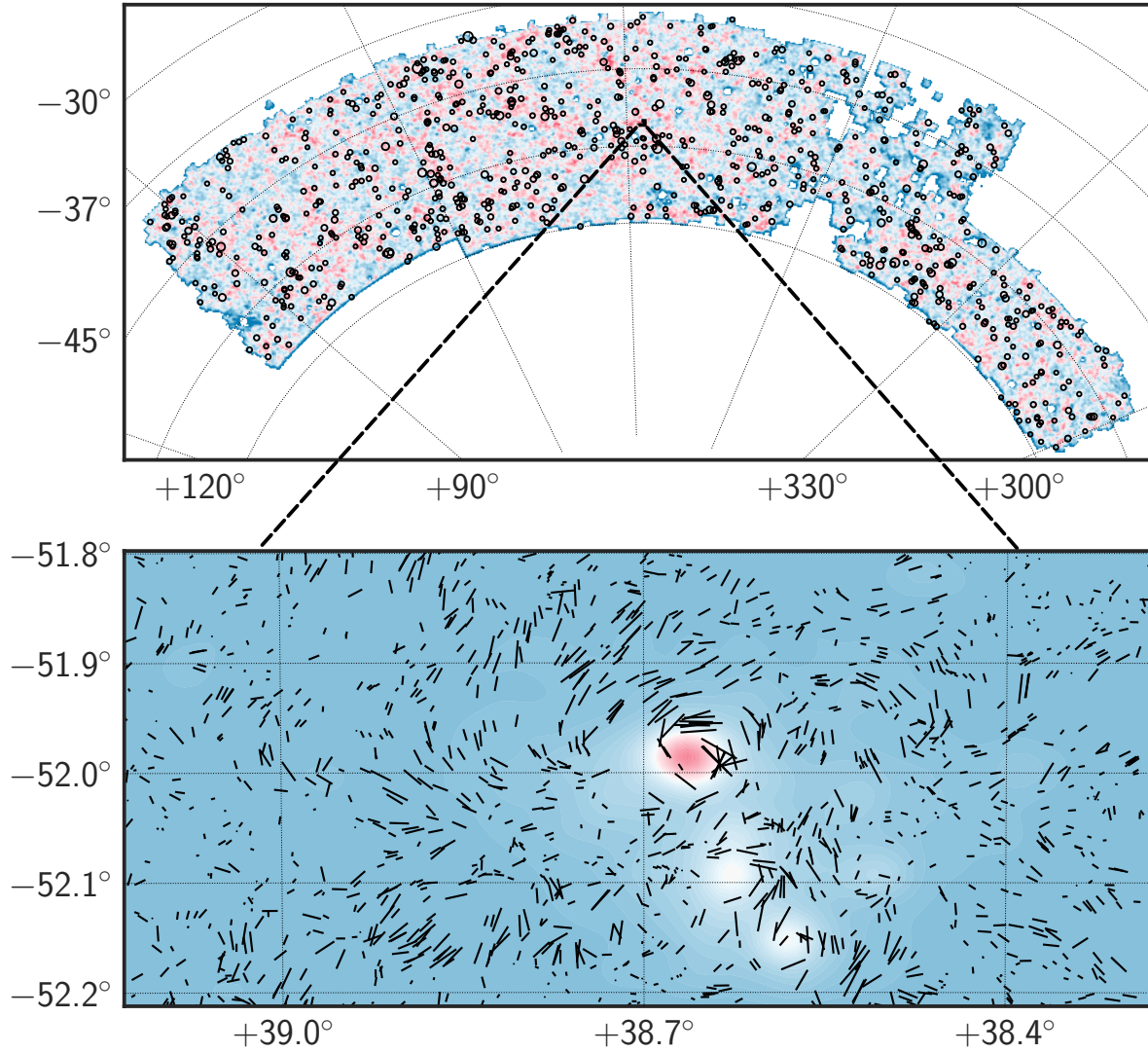


Figure 1. A synthetic Dark Energy Survey sky. *Top:* Projected matter density field of one Buzzard footprint, corresponding to the SPT area of the DES Y1 footprint, with $\lambda > 50$ redMaPPer clusters plotted as the black circles. Many analyses have used only the portion of this footprint with RA < 300 . *Bottom:* Zoom in of a massive halo. The color map represents matter density and black whiskers are the direction and amplitude of the true shear of background galaxies in our simulated Y1 weak-lensing catalogs.

analyses, including cosmic shear, galaxy–galaxy lensing, angular clustering and the combination thereof, called a 3×2 -point analysis. Measurements of galaxy cluster abundances will also be a powerful cosmological probe in DES (Weinberg et al. 2013; Costanzi et al. 2019). For this reason, we will focus on comparisons between our simulations and the most important quantities for these analyses in this work. In particular we will focus on four main galaxy samples in this paper:

- A sample of galaxies with photometric errors and photometric redshifts approximating the GOLD sample.
- The REDMAGIC sample, which was used as a lens galaxy sample in DES Collaboration et al. (2017).
- A weak-lensing source sample, approximating the METACALIBRATION sample used in DES Collaboration et al. (2017).
- The REDMAPPER photometric cluster sample.

The GOLD catalog is the parent catalog of reliable galaxy detections from which all other galaxy samples are selected for DES analyses (Drlica-Wagner et al. 2018). The REDMAGIC (Roza et al. 2016) and REDMAPPER catalogs (Rykoff et al. 2014) are photometrically selected luminous red galaxy and cluster samples. The REDMAGIC sample has been optimized to provide accurate red–sequence–based photometric redshifts and a constant comoving number density. Likewise, the REDMAPPER cluster sample has been optimized to have accurate photometric redshifts, and the richness, λ , associated with every cluster is a low-scatter halo mass proxy (McClintock et al. 2018). The METACALIBRATION sample in the DES Y1 data is a subsample of the GOLD catalog with robust ellipticity measurements, made using the METACALIBRATION shear measurement algorithm (Sheldon & Huff 2017; Huff & Mandelbaum 2017), that can be used in the measurement of weak-lensing statistics (Zuntz et al. 2018).

When showing measurements for the samples listed above, we will typically use the redshift bins from DES Collaboration et al. (2017), i.e. five lens bins and four source bins for REDMAGIC and our weak-lensing source sample respectively. In this section we define a number of observables that we wish to model and discuss the process by which they are included in our simulations in the next section.

2.1. Galaxy Clustering

As a photometric survey, the primary clustering statistic used in DES is angular clustering. In particular we are interested in auto- and cross correlations of a galaxy sample binned tomographically by redshift. Assuming the Limber approximation (Limber 1954), which is appropriate for the

broad redshift binning used for DES observables, and following the notation in Krause et al. (2017), the angular clustering signal is given by:

$$w^{i,j}(\theta) = \int \frac{dl l}{2\pi} J_0(l\theta) \int d\chi \frac{q_{\delta_g}^i\left(\frac{l+1/2}{\chi}, \chi\right) q_{\delta_g}^j\left(\frac{l+1/2}{\chi}, \chi\right)}{\chi^2} \times P_{\text{NL}}\left(\frac{l+1/2}{\chi}, z(\chi)\right), \quad (1)$$

where the radial weight function for clustering in terms of the comoving radial distance χ is

$$q_{\delta_g}^i(k, \chi) = b^i(k, z(\chi)) \frac{n_g^i(z(\chi)) dz}{\bar{n}_g^i d\chi}, \quad (2)$$

where J_0 is the 0th order Bessel function, redshift distributions given by $n_g^i(z)$, $b^i(k, z(\chi))$ denoting the bias of the galaxies in tomographic bin i , $P_{\text{NL}}(k, z)$ the non-linear matter power spectrum at wave number k and redshift z , and average angular number densities given by:

$$\bar{n}_g^i = \int dz n_g^i(z). \quad (3)$$

A number of important details which must be modeled in our simulations become apparent, including non-linear evolution of the matter distribution, scale-dependent galaxy bias, and galaxy redshift distributions.

2.2. Galaxy Lensing

We also wish to model the weak-lensing statistics most commonly used in DES. In this paper we will discuss measurements of cosmic shear and galaxy–galaxy lensing. Cosmic shear auto- and cross-correlation functions can be expressed as two two-point correlation functions:

$$\xi_{+/-}^{ij}(\theta) = (1+m^i)(1+m^j) \int \frac{dl l}{2\pi} J_{0/4}(l\theta) \int d\chi \frac{q_{\kappa}^i(\chi) q_{\kappa}^j(\chi)}{\chi^2} P_{\text{NL}}\left(\frac{l+1/2}{\chi}, z(\chi)\right), \quad (4)$$

where m^i is the multiplicative bias of the shear estimates in the i th tomographic bin, $J_{0/4}(l\theta)$ are 0th and 4th order Bessel functions. The lensing kernel, q , is given by

$$q_{\kappa}^i(\chi) = \frac{3H_0^2 \Omega_m}{2c^2} \frac{\chi}{a(\chi)} \int_{\chi}^{\chi_h} d\chi' \frac{n_{\kappa}^i(z(\chi')) dz/d\chi'}{\bar{n}_{\kappa}^i} \frac{\chi' - \chi}{\chi'}, \quad (5)$$

with the Hubble constant given as H_0 , c the speed of light, and a the scale factor. Tangential shear–galaxy cross correlations, often referred to as galaxy–galaxy lensing, can be expressed as:

$$\gamma_t^{ij}(\theta) = (1+m^j) \int \frac{dl}{2\pi} J_2(l\theta) \int d\chi \frac{q_{\delta_g}^i\left(\frac{l+1/2}{\chi}, \chi\right) q_{\kappa}^j(\chi)}{\chi^2} \times P_{\text{NL}}\left(\frac{l+1/2}{\chi}, z(\chi)\right). \quad (6)$$

We have included multiplicative bias in these expressions for completeness only, as we do not model this in these simulations. Again, we see that galaxy bias and the non-linear matter power spectrum are key ingredients in these observables and thus must be accurately modeled in our simulations. In principle, baryons affect the matter power spectrum at small scales, but the DES cosmology analyses have made conservative scale cuts in order to mitigate these effects.

2.3. Cluster Counts

Finally, we wish to model the number densities of clusters as a function of richness, λ , an observable that is tightly correlated with the dark matter halo mass of these clusters, and redshift:

$$n(\Delta\lambda_i, z) = \int_0^\infty dM n(M, z) \int_{\Delta\lambda_i} d\lambda p(\lambda|M, z), \quad (7)$$

where $\Delta\lambda_i$ represents a bin in richness, $n(M, z)$ is the number density of halos as a function of mass and redshift, and $p(\lambda|M, z)$ is the probability that a halo of mass M has observed richness λ , also known as the mass–richness relation, or mass–observable relation (MOR). Accurate modeling of the halo mass function and mass–richness relation are necessary in order to reproduce observed cluster number counts.

3. CREATING SYNTHETIC DARK ENERGY SURVEYS

A brief summary of the algorithm steps are as follows:

1. Determine matter distribution (§3.1):
 - (a) run N-body simulations, output lightcones for large-volume simulations and snapshots for high-resolution simulations
 - (b) find dark matter halos
 - (c) run merger tree on high-resolution simulations
 - (d) calculate densities on halo centers; calculate densities on particles for large volume boxes
2. Add galaxies (§3.3):
 - (a) calibrate luminosity-density relation in the SDSS $z = 0.1$ frame r -band on a high-resolution tuning simulation using abundance matching to predict the galaxy distribution

- (b) add galaxies to large volume lightcones, based on luminosity-density relation
- (c) measure the observed distribution of SEDs at a given luminosity and galaxy density in SDSS and use to assign SEDs to simulated galaxies

3. Lens galaxies (§4.1):

- (a) add unlensed galaxy shapes and sizes
- (b) calculate lensing fields (shear, deflection, convergence, rotation) via ray-tracing at all galaxy positions
- (c) lens (magnify and distort) galaxies, including multiple images

4. “Observe” galaxies (§3.4 and §4.1):

- (a) rotate into DES footprint, apply survey mask
- (b) apply photometric errors
- (c) calculate photometric redshifts
- (d) select samples

The final result is a synthetic galaxy catalog containing positional, spectroscopic, and photometric information, as well as additional properties such as photometric redshift information. In addition, the catalog contains measured properties of the matter distribution, including halo properties and weak-lensing quantities. Fig. 1 shows an example of one of our simulations, displaying the underlying projected matter distribution, an observed cluster catalog and weak-lensing shear around a massive cluster. A full list of modeled galaxy properties appears in Appendix A.

3.1. N-body Simulation Methodology

The key details of the simulations run are listed in Table 1. The simulations L1, L2, and L3 are combined to build the particle lightcone that generates 10,313 square degrees of unique, contiguous sky. The box T is used to tune the galaxy assignment algorithm as described below and thus only one per cosmological model is needed. Note that at higher redshifts in a flux-limited survey, the smallest halo mass needed to model a given set of galaxies increases, since progressively higher luminosity galaxies living in more massive halos are probed at higher redshifts. Thus, using simulation volumes of progressively lower resolution as a function of redshift in the lightcone allows us to lower the computational cost of the simulations. The disadvantage of this technique is that it leaves discontinuities in cosmic structures along the line-of-sight at the edges between the different lightcones. We have placed the transitions in redshift where typical red sequence galaxy photometric redshifts have worse performance due the 4000 Å moving between filters (Rykoff et al. 2014).

Table 1. Description of the simulations used to create the particle lightcone.

Name	z_{min}	z_{max}	L_{box}	N_{part}	m_{part}	$\epsilon_{Plummer}$	$M_{r,lim}$	N_{halos} w/ 50 particles	$N_{galaxies}$ to DES limit
T	tuning only	tuning only	400 h^{-1} Mpc	2048 ³	$4.8 \times 10^8 h^{-1} M_{\odot}$	5.5 h^{-1} kpc	–	5.3M	NA
L1	0.0	0.32	1.05 h^{-1} Gpc	1400 ³	$3.3 \times 10^{10} h^{-1} M_{\odot}$	20 h^{-1} kpc	-10	4.7M	1×10^8
L2	0.32	0.84	2.6 h^{-1} Gpc	2048 ³	$1.6 \times 10^{11} h^{-1} M_{\odot}$	35 h^{-1} kpc	-16.6	8.2M	3×10^8
L3	0.84	2.35	4.0 h^{-1} Gpc	2048 ³	$5.9 \times 10^{11} h^{-1} M_{\odot}$	53 h^{-1} kpc	-19.1	1.4M	3×10^8

Briefly, we use 2LPTIC (Crocce et al. 2006) and L-GADGET2 (Springel 2005) to initialize and run our simulations. We use a Λ CDM cosmology with $\Omega_m = 0.286$, $h = 0.7$, $\sigma_8 = 0.82$, $n_s = 0.96$, and $\Omega_b = 0.046$, with three massless neutrino species and $N_{eff} = 3.046$. We refer to this as the Buzzard cosmology, hence the name of the simulation suite. We have made further specialized modifications to the codes to initialize simulations of generic dark energy models using second-order Lagrangian perturbation theory and to generate lightcone outputs on-the-fly. We find halos with ROCKSTAR (Behroozi et al. 2013a) and generate merger trees on our high resolution simulation with CONSISTENT-TREES (Behroozi et al. 2013b). Finally, we use CALCLENS (Becker 2013) to compute the weak-lensing shear, magnification and lensed galaxy positions from the lightcone outputs. The full details of our N-body and simulation post-processing methodology are described in Appendices B, C, and D.

3.2. N-body simulation validation

We have compared our simulations to standard fitting functions and analytic approximations, the results of which are shown in Figs. 2 and 3. As seen in Fig. 3, the power spectra, $P(k)$, in both the L1 and L2 boxes agree with the predictions from the COSMICEMU emulator within their quoted errors (4%; Lawrence et al. 2017) for wavenumbers $k < 2 h^{-1}$ Mpc (left panel). We see poor agreement above scales of $k = 2 h^{-1}$ Mpc in the L2 box. The matter in the L3 box is weighted significantly less by the lensing kernel of typical DES source galaxies, making its contribution to weak-lensing observables small, and so is not shown. However, as discussed in Appendix C and demonstrated in the right panel of Fig. 3, the weak-lensing signals from our simulations, presented here in the form of $\xi_{+/-}$ measured without shape noise and averaged over all 18 simulations, are affected by the relatively lower resolution of the L2 and L3 boxes.

Similarly, we find that the L1 and L2 boxes agree with halo mass function and halo bias predictions in the literature (McClintock et al. 2018; Tinker et al. 2010), as seen in the left and right panels of Fig. 2 respectively. The $\sim 1\%$ deviations seen in the mass function are due the differences in halo definition used in our simulations and that used in McClintock et al. (2018) as described in Appendix B.3. The halo mass func-

tion of L3 is again affected by the lower resolution of this box, but the vast majority of clusters detected in DES have redshifts $z < 0.9$, as the red sequence used to find clusters redshifts out of the DES bands at this point, and more generally becomes less well defined above $z = 1$. Thus, the impact of resolution effects in L3 on photometrically detected cluster observables is negligible, although it may be important for cluster selections that are less redshift dependent such as those based on the thermal Sunyaev-Zel’dovich effect (e.g. Bleem et al. 2015).

Both the resolution effects and the discontinuities in the matter distribution were shown to have negligible impact on inferring the true cosmology of these simulations using a 3×2 -point analysis with a DES Y1 covariance matrix in MacCrann et al. (2018). This statement is analysis dependent, and analyses that use smaller scales, or that have smaller errors on their observables, such as DES Y3 and Y5 analyses, may not be immune to systematic effects due to the compromises made in creating these simulations. See Appendices B and C for additional discussion.

3.3. Building Galaxy Populations: ADDGALS and the Color-Density Relationship

We use the ADDGALS algorithm to populate our lightcones with galaxies. We briefly describe the algorithm here and refer the reader to Wechsler et al. (2019) for more details. Additional implementation details related to high redshift extensions of the ADDGALS model are presented in Appendix E.

ADDGALS uses three main distributions to populate galaxies:

- A luminosity function, $\phi(M_r, z)$
- The distribution of central galaxy absolute magnitude at fixed halo mass and redshift, $P(M_{r, cen} | M_{vir}, z)$
- The distribution of galaxy overdensities conditioned on absolute magnitude and redshift, $P(R_{\delta} | M_r, z)$, where R_{δ} is the radius around each galaxy enclosing $1.3 \times 10^{13} h^{-1} M_{\odot}$.

These PDFs are measured by applying a SHAM model to the T1 simulation, using a luminosity function, $\phi(M_r, z)$, determined from data as described below. In order to determine

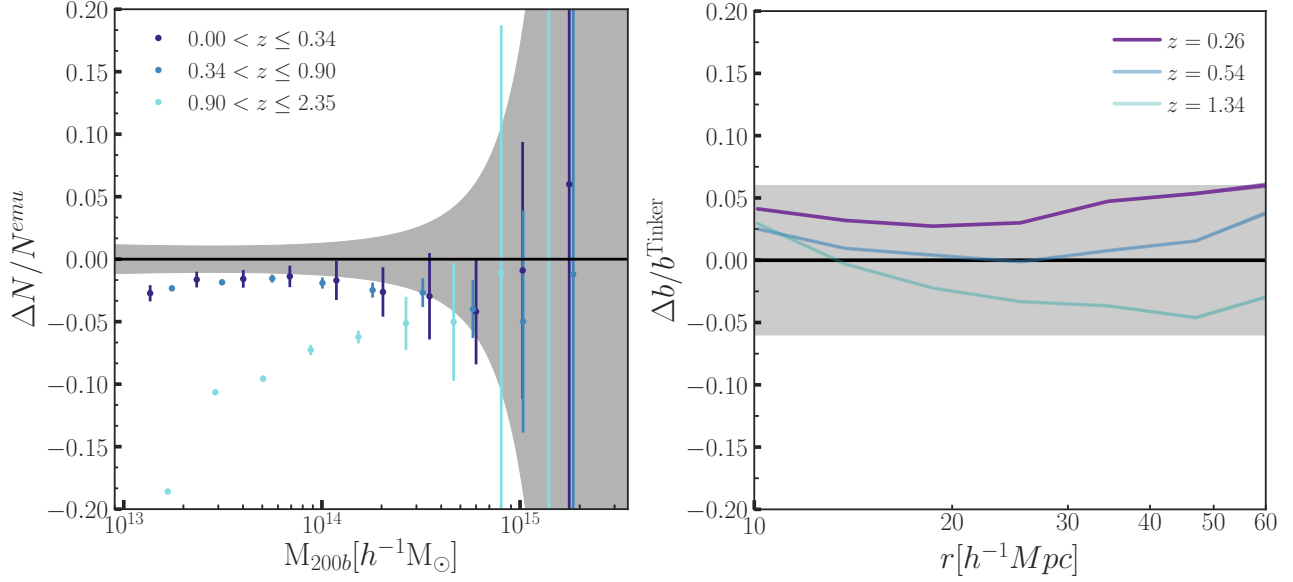


Figure 2. *Left:* The fractional error in the halo mass function measured from the mean of our simulations with respect to the McClintock et al. (2018) halo mass function emulator. The three redshift bins correspond to the L1, L2 and L3 simulations from low to high redshift. The grey band represents the accuracy requirement for DES Y5 at $z=0.5$ as computed in McClintock et al. (2018). The accuracy of the emulator is better than this at all masses. The discrepancies at $z < 0.9$ are likely due to differences in halo definition (see discussion in Appendix B.3). The discrepancies seen at high redshift, where the emulator over-predicts the simulations, are due to resolution effects in the L3 lightcone. *Right:* Fractional error of halo bias measured in a bin with mean mass of $4 \times 10^{13} h^{-1} M_{\odot}$ for three different redshifts (lines) with respect to the predictions from Tinker et al. (2010). The measurements are averaged over all L1, L2 and L3 simulations for the first, second and third redshift bin respectively. The grey band represents the quoted 6% error in the Tinker et al. (2010) predictions.

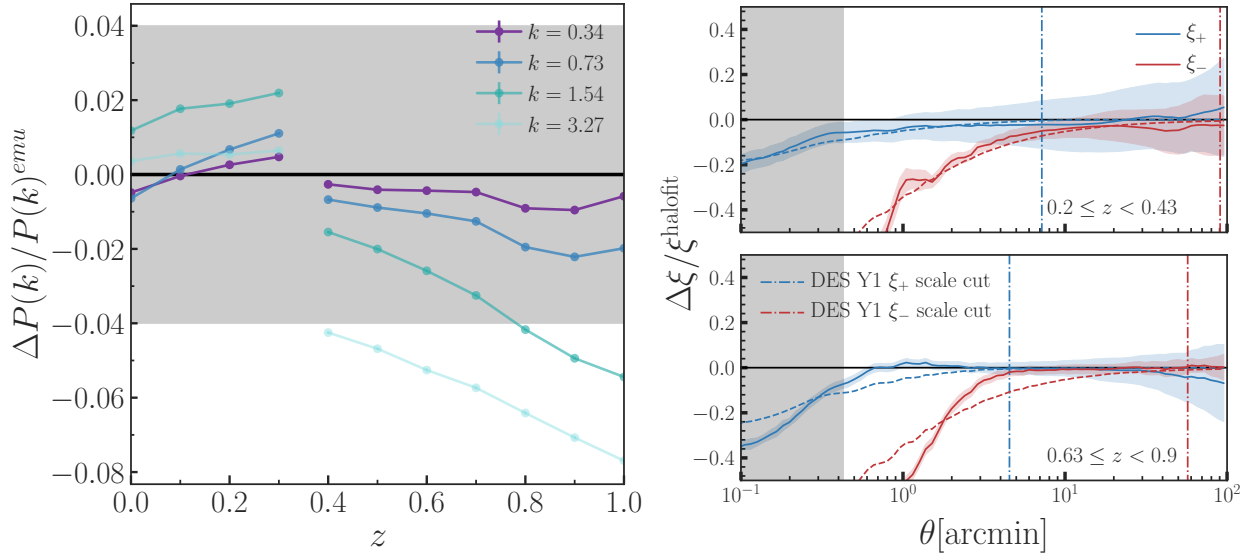


Figure 3. *Left:* Ratio of the the matter power spectrum measured in snapshots of the L1 (for $z < 0.35$) and L2 (for $z > 0.35$) simulations to the CosmicEmu (Lawrence et al. 2017) as a function of redshift for different values of k . L3, not shown, is used for $z > 0.9$ and is lower resolution than L2. The switch between L1 and L2 is marked by a break in the lines. *Right:* Comparison of $\xi_{+/-}$ (blue/red) without shape noise (solid) to halo fit (dashed) for two different redshift bins averaged over 18 Y1 footprints (top panel). The fractional deviation from halo fit (Takahashi et al. 2012) (dashed) compared to the prediction made using a halo fit power spectrum truncated at a fixed ℓ approximately corresponding to the ray-tracing resolution is shown in the bottom panel. The different scale dependence of the resolution effects in the two redshift bins indicates that they are due to the resolution of the underlying N-body simulation and not the ray-tracing. The gray region corresponds to the approximate angular resolution of the HEALPix grid used to perform the ray-tracing.

$P(M_{r,\text{cen}}|M_{\text{vir}}, z)$ we fit a functional form to the mean relation in the SHAM and assume Gaussian scatter around that, i.e.

$$P(M_{r,\text{cen}}|M_{\text{vir}}) = \mathcal{N}(M_{r,\text{cen}}(M_{\text{vir}}), \sigma_{M_{r,\text{cen}}}). \quad (8)$$

$P(R_\delta|M_r, z)$ is determined by measuring R_δ around each simulated galaxy in the SHAM catalog and measuring the distribution of R_δ for galaxies above a given magnitude cut, M_r , in a snapshot with redshift z . A functional form is then fit to this distribution as a function of M_r and z .

We use the best-fit SHAM model from [Lehmann et al. \(2017\)](#), which postulates, roughly, that brighter galaxies live in halos with higher peak circular velocities, while allowing for some scatter in the v_{peak} - luminosity relation. It has been shown to reproduce the luminosity dependent clustering as measured in SDSS to high precision (e.g. [Conroy et al. 2006a](#); [Reddick et al. 2013](#); [Lehmann et al. 2017](#)). For more details about the SHAM model that we use, and how $P(R_\delta|M_r, z)$ is determined we direct the reader to [Wechsler et al. \(2019\)](#).

In order to assign galaxies to our lightcones, we first assign central galaxies to resolved halos using the $P(M_{r,\text{cen}}|M_{\text{vir}}, z)$ defined by the SHAM. Doing so only accounts for a small fraction of the galaxies observed by a survey such as DES. To populate our lightcones with the remaining galaxies, we use the $P(R_\delta|M_r, z)$, drawing a galaxy from the observed luminosity function and an overdensity for this galaxy from $P(R_\delta|M_r, z)$, and assigning it to a dark matter particle with the correct overdensity R_δ . This procedure results in a galaxy catalog that matches the scale- and luminosity-dependent two-point clustering in a single magnitude band. We choose to assign galaxies to particles as they are convenient points around which to measure densities, but in principle we can place galaxies anywhere the local densities required for the method can be measured. Using particles places a limit on the number density of galaxies that we can assign, but the catalogs here do not approach this limit.

The above procedure results in a catalog with a single absolute magnitude per galaxy. We also wish to assign SEDs to each galaxy. Doing so involves two additional observational inputs:

- A training set of galaxies from which to draw SEDs
- The fraction of galaxies that are red at fixed M_r and z

We assign SEDs from the SDSS DR7 VAGC ([Blanton et al. 2005b](#)) to our simulated galaxies by imposing that our simulation match the SED–luminosity–density relationship measured in the SDSS data. The evolution in this relationship is calibrated to the evolution of the red fraction of galaxies from PRIMUS ([Coil et al. 2011](#)) as a function of M_r and z . The relatively small area of PRIMUS, 9 sq. degrees, may contribute non-negligible sample variance to this relation, but its unpar-

alleled spectroscopic depth of $r \sim 23.5$ makes it ideal for the purposes of this calibration.

In more detail, the assignment of galaxy SEDs proceeds by measuring the projected distance to the fifth nearest neighbor, Σ_5 , in a small bin in redshift around each galaxy in both the the SDSS DR7 VAGC and our mock catalog. We sort these distances producing a *rank* R_{Σ_5} . We then assign SEDs to each mock galaxy by selecting a galaxy from the data in the same bin of absolute magnitude M_r and R_{Σ_5} . Evolution in the SED–luminosity–density relation is accounted for by preferentially drawing from blue galaxies over red ones at higher redshifts, enforcing the constraint that the red fraction of galaxies match that measured in PRIMUS as a function of luminosity and redshift. The assumptions made by this method do not hold in detail, and the resulting imperfections are discussed below. SEDs are represented as weighted sums of 5 KCORRECT ([Blanton & Roweis 2007](#)) templates, allowing for efficient computation of the intrinsic observed magnitudes of each mock galaxy in a variety of pass bands. See [Appendix E.2](#) for more details.

The above procedure relies on a measurement of the galaxy luminosity function in the data over the range of redshifts of interest. This task is non-trivial given the large number of systematic effects in the measurement of galaxy magnitudes, survey incompleteness, redshift errors, and other systematics. Further, we would like our luminosity function, when integrated over a typical Λ CDM volume, to match the observed DES Y1 galaxy counts as a function of magnitude. To complete this task, we start with a luminosity function as measured with small statistical error at low redshift using the method described in [Reddick et al. \(2013\)](#) based on the SDSS spectroscopic sample. To account for redshift evolution we fit for an additive evolution in M_* by first populating a full lightcone using our fiducial luminosity function and then minimizing the difference between our fiducial counts in the DES Y1 bands and the observed counts in the $\approx 1.5 \text{ deg}^2$ overlap between DES and COSMOS, which is approximately 1 magnitude deeper than the wide field observations. This correction is described in more detail in [Appendix E.1](#).

The final magnitude counts and the color distributions of our mock galaxies compared to the DES Y1 data are shown in [Figs. 4, 5 and 6](#). We find that our catalogs are in agreement with measurements of DES counts to $\sim 10\text{--}20\%$ accuracy depending on the band as can be seen in [Fig. 4](#), and are roughly consistent with a power-law extrapolation to fainter magnitudes, represented by the dashed lines in that figure. At $i = 24$ we expect $\sim 10\%$ under-predictions in counts due to the fact that we are not populating galaxies with $z > 2.35$, with the deficit becoming worse at fainter magnitudes. Residual discrepancies between the different bands are due to the fact that colors in these simulations become redder than what is observed in the data at high redshift (see

the discussion below), leading to relative underestimates of $\bar{n}(> \bar{m})$ for bluer bands. The regime brighter than shown in Fig. 4 matches counts in the SDSS main sample to $\sim 10\%$ as shown in Wechsler et al. (2019). These deviations are small enough to allow for the generation of photometric cluster and LRG samples that provide reasonable facsimiles of a number of statistics as measured in the DES Y1 data as discussed in 4.2 and 4.3.

The Figs. 5 and 6 show the distribution of colors in Buzzard compared to those measured in the DES overlap with COSMOS in a magnitude bin of $18 < m_r < 23$. Brighter than this, our colors are well validated by SDSS, and fainter than this, the COSMOS overlap with DES has large photometric noise and is likely incomplete. We bin the COSMOS galaxies by redshift using their BPZ photometric redshifts which have significantly smaller dispersion than the size of the redshift bins used here (Laigle et al. 2016). At low redshift, the colors show relatively small deviations from those in the data, a non-trivial accomplishment given that the apparent magnitude range probed here is significantly deeper than that used in our training set ($m_r < 17.7$). At higher redshifts, we see two main modes of deviation between COSMOS and Buzzard. The first is that the mean of the blue sequence of galaxies is significantly bluer in the data than in the simulations. To demonstrate this we have also plotted Buzzard colors where we have shifted the mean of the blue sequence in each redshift bin separately for each color to match the COSMOS data. Error bars on the shifted distribution in Fig. 5 are calculated via jackknife on 128 COSMOS sized patches in Buzzard. The agreement between this shifted Buzzard distribution and distribution of colors in COSMOS is much better. This is significant, as it means that improving the colors dramatically in these simulations may be a matter of including relatively minor adjustments to our templates as a function of redshift, rather than incorporating additional templates. Kolmogorov-Smirnov (KS) tests comparing the 1D COSMOS distributions and shifted Buzzard colors still reject the null hypothesis (that the distributions are drawn from the same underlying distribution) at high significance, but the KS statistics improve drastically between the unshifted and shifted distributions in nearly all cases. The other main difference is that at high redshift the width of the red sequence in $g-r$ and $r-i$ is greater in the data than in the simulations. Given that we do not make any effort to evolve our templates using stellar evolution models, it is possible that taking this into effect may resolve some of the discrepancies seen here.

The level of agreement between the simulations and the data in this space has allowed us to run a number of algorithms that rely on reproducing the color-redshift relation in the data, such as photometric redshift and sample selection algorithms. The performance of these on the simulations is discussed below, but in general they produce re-

sults which have many of the qualitative features observed in the data, while failing to match in a rigorous statistical sense. Nonetheless, the photometric redshifts and color selected samples in these simulations have proven useful for a number of studies (e.g. MacCrann et al. 2018).

To summarize, the free parameters of the model are the following:

1. The luminosity proxy and scatter assumed in the abundance matching procedure used to tune the ADDGALS method
2. An r -band luminosity function and its evolution with redshift
3. The catalog of galaxies from which SEDs are drawn
4. The red fraction of galaxies as a function of absolute magnitude and redshift

and the following data sets are used to tune each of these parameters respectively:

1. Luminosity-dependent projected clustering in the SDSS DR7 VAGC
2. The luminosity function of the SDSS DR7 VAGC and $\bar{n}(> \bar{m})$ in DES Y1
3. SDSS DR7 color distributions
4. The red-fraction of galaxies as a function of absolute magnitude and redshift in PRIMUS

We have not listed $p(R_\delta|M_r, z)$ as a free parameter as it is fully specified by the assumed SHAM model and our fitting procedure.

3.4. Masking and Observational Effects

Once we have populated a lightcone with galaxies and lensed them, we apply several post-processing steps to approximate the effects of the DES Y1 image processing pipeline, including the effects of masking and the reported DES Y1 observing conditions. First, we cut out two different kinds of DES Y1 footprints from catalogs, one (1120 sq. degrees) by excluding $330 < \text{RA}$ and the S82 region of the footprint, the region of the footprint overlapping with SDSS Stripe 82, and the other by using all area not including the S82 region (1321 sq. degrees). We are able to produce six of the reduced footprint and two of the full footprint per lightcone simulation. Second, we apply the DES Y1 footprint mask, including all areas with greater than one exposure. We then randomly downsample the galaxies according the quantity FRACGOOD of the Y1 footprint mask, which describes the amount of masking at scales below the resolution of the

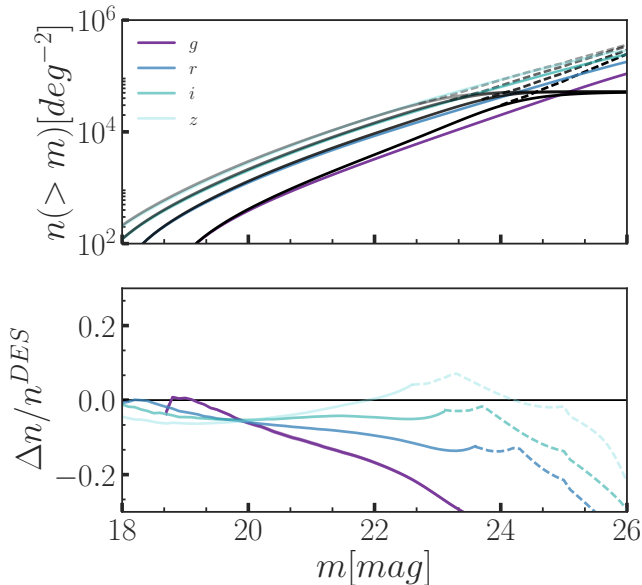


Figure 4. (top) Cumulative number of observed galaxies as a function of true magnitude per square degree in Buzzard (colors) compared to the same quantity as a function of observed magnitude in the DES Y1 wide field data (solid black) and a power law extrapolation to fainter magnitudes (dashed black). (bottom) Fractional deviation of the simulations from the data and its power law extrapolation with Poisson error bars which are mostly not visible due to their small amplitude. At magnitudes fainter than $r = 24$, we expect $> 10\%$ deficits in Buzzard due to the absence of galaxies with $z > 2.35$.

masks. Finally, we use maps of the $10\text{-}\sigma$ limiting magnitude and the effective exposure time to apply photometric noise to the galaxy magnitudes assuming Poisson sampling statistics to account for errors due to background sky photons as well as photons intrinsic to the galaxy itself. See Appendix E for details.

4. COMPARISON TO DES Y1 OBSERVATIONS

We now compare the suite of mock catalogs to various quantities measured in the DES Y1 survey. These include photometric redshifts, cosmic shear, galaxy–galaxy lensing, galaxy clustering, and optically-identified galaxy clusters.

4.1. Photometric Redshifts and Cosmic Shear

We calculate photometric redshifts for each object using BPZ (Benítez 2000), the primary photometric redshift code used in the DES Y1 analyses. The same BPZ configuration as used in the Y1 data is applied to the simulations. In particular we use the same template SEDs as described in Hoyle et al. (2018) and the bandpasses and photometric calibration uncertainties described in Drlica-Wagner et al. (2018). In Fig. 7, we show the characteristic error and bias on the BPZ redshifts as a function of magnitude and z_{BPZ} for all galaxies detected in our DES Y1 catalogs after applying the error model described in Appendix E.4.

In order to facilitate analyses requiring a Y1-like source galaxy sample, we have selected a sample of galaxies from our simulations matched to the DES Y1 METACALIBRATION sample. The DES Y1 METACALIBRATION sample is the main shear catalog used in the DES Y1 3×2 point analyses. This is a subsample of the DES Y1 GOLD catalog (Drlica-Wagner et al. 2018) selected to have robust ellipticity measurements that can be used in the measurement of weak-lensing statistics. The shape measurement and subsequent selection algorithm is described in Zuntz et al. (2018). As we do not perform image simulations using our simulated catalogs, we cannot select a shear catalog in the same way as is done in the data. Instead, we have chosen to select galaxies with similar signal-to-noise properties as found in the data by performing the following cuts:

1. Mask all regions of the footprint where limiting magnitudes and PSF sizes cannot be estimated.
2. $\sigma(m_{r,i,z}) < 0.25$
3. $\sqrt{r_{gal}^2 + (0.5 r_{PSF})^2} > 0.75 r_{PSF}$
4. $m_r < 20.88 + 2.89 z$

where $\sigma(m_{r,i,z})$ are the magnitude errors in riz bands and r_{PSF} is the r -band PSF FWHM estimated from the data at the position of each galaxy. r_{gal} is the half light radius of the galaxy. The first three cuts are well motivated physically and intended to approximate signal-to-noise cuts imposed either explicitly or implicitly in shape catalog production on the data. These cuts yield a shape catalog that has too many galaxies compared to the data, possibly due to the fact that we have neglected to incorporate the dependence of photometric errors and detection on surface brightness into our photometric error model. The fourth cut is necessary to match the number density of sources in the four source redshift bins used in the DES Y1 key project, yielding values for the shot noise, σ_e^2/n_{eff} , in each bin of 0.050, 0.053, 0.047, 0.11, compared to 0.046, 0.059, 0.046, and 0.11 for the METACALIBRATION catalog on the Y1 data.

The extent to which this selection matches the DES Y1 METACALIBRATION redshift distributions can be seen in Fig. 7. Qualitatively, the shape of the BPZ redshift distributions match those found in the data, but there are some quantitative differences. The mean redshift in each source bin as estimated by BPZ on Buzzard is 0.368, 0.515, 0.762, and 1.04 while for the DES Y1 METACALIBRATION sample they are 0.389, 0.525, 0.743 and 0.966. The differences in the mean redshifts of the four tomographic bins are statistically significant, with the errors on the mean in both the simulations and the data being on the order of 10^{-4} . Having the true redshifts for every galaxy in our simulations, we can also compute the bias in this

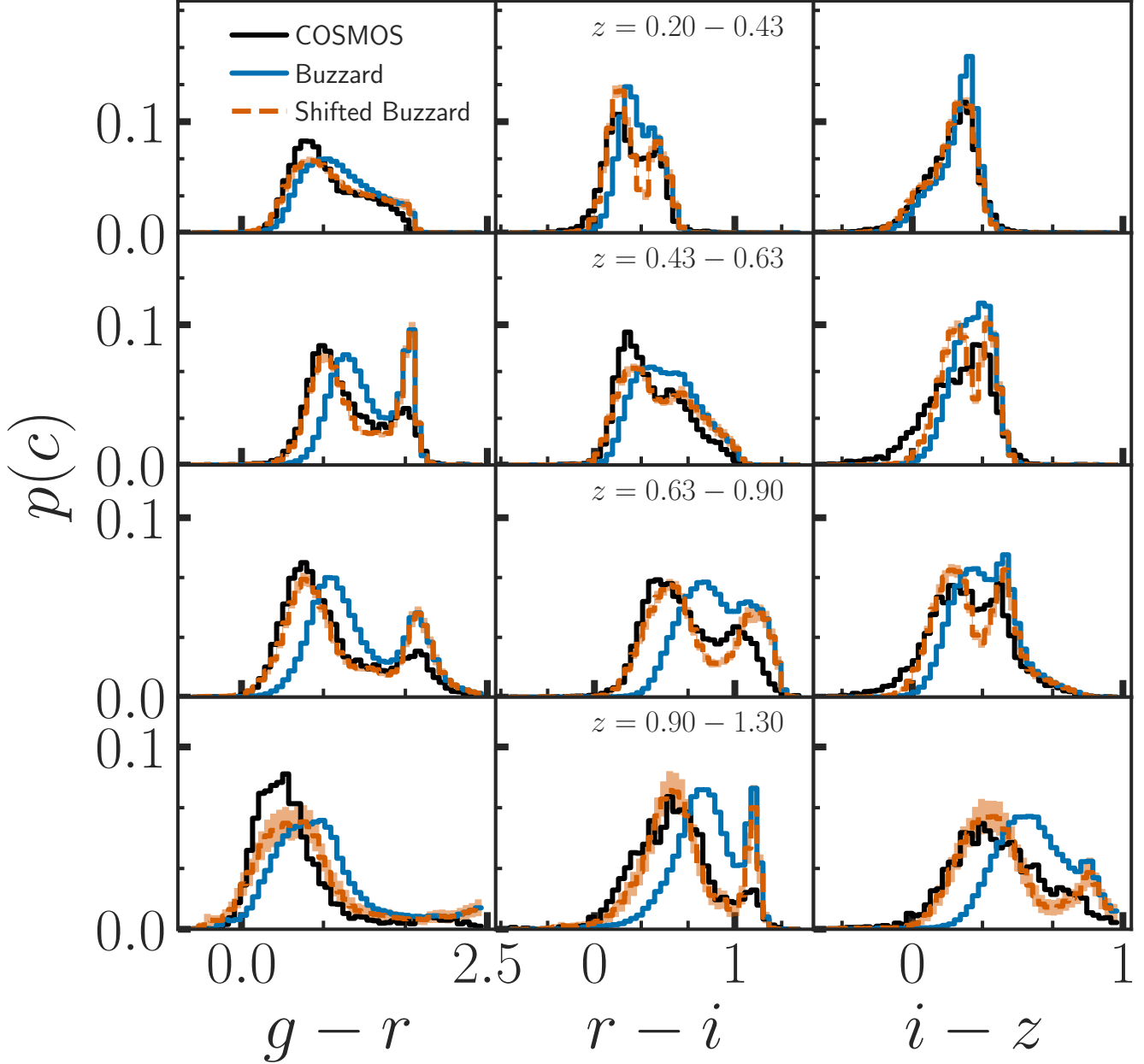


Figure 5. Comparison of the $g-r$, $r-i$ and $i-z$ colors between Buzzard and COSMOS for magnitudes $18 < m_r < 23$ in the redshift bins used for source galaxies in the Y1 3×2 point analysis. Dashed orange lines represent Buzzard colors where we have shifted the mean of the blue sequence in each redshift bin to match the observed colors. The significant improvement in the agreement between the shifted Buzzard distribution and COSMOS shows that the most relevant difference between COSMOS colors and Buzzard is just such a shift. Error bars are estimated via jackknife from 128 COSMOS sized patches in Buzzard.

mean for each source bin, yielding offsets of 0.052, 0.023, -0.0037, 0.0061. These biases were also estimated in the data and found to be -0.001 ± 0.016 , -0.019 ± 0.013 , 0.009 ± 0.011 , and -0.018 ± 0.022 (Hoyle et al. 2018; Davis et al. 2017; Gatti et al. 2018).

Comparisons of $\xi_{+/-}$ between Buzzard and the DES Y1 data can be seen in Fig. 8. We refrain from making any statistical comparisons between these sets of measurements as

our intent was not necessarily to fit this data, but note that in general the qualitative agreement between them is good. Differences in cosmology between our simulations and the Universe could contribute to the minor differences here, but coincidentally the Buzzard cosmology is quite close to the best fit cosmology as measured in DES Collaboration et al. (2017).

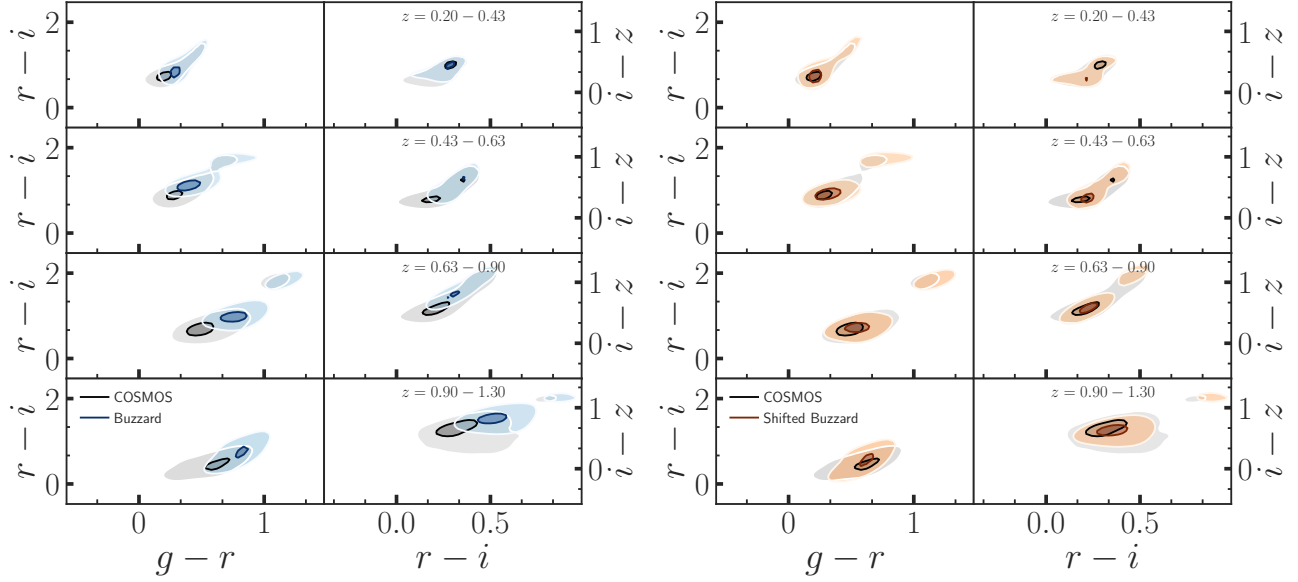


Figure 6. (left) Comparison of two dimensional color distributions between Buzzard and COSMOS for magnitudes $18 < m_r < 23$ in the redshift bins used for source galaxies in the Y1 3×2 point analysis. The left column is the joint distribution of $g-r$ and $r-i$ colors and the right is $r-i$ and $i-z$. Contours represent the one and two sigma boundaries of the distributions. (right) The same, but for Buzzard colors with the blue cloud shifted in the same way as in Fig. 5. Again, the significant improvement in the agreement between the shifted Buzzard distribution and COSMOS shows that the most relevant difference between COSMOS colors and Buzzard is just such a shift.

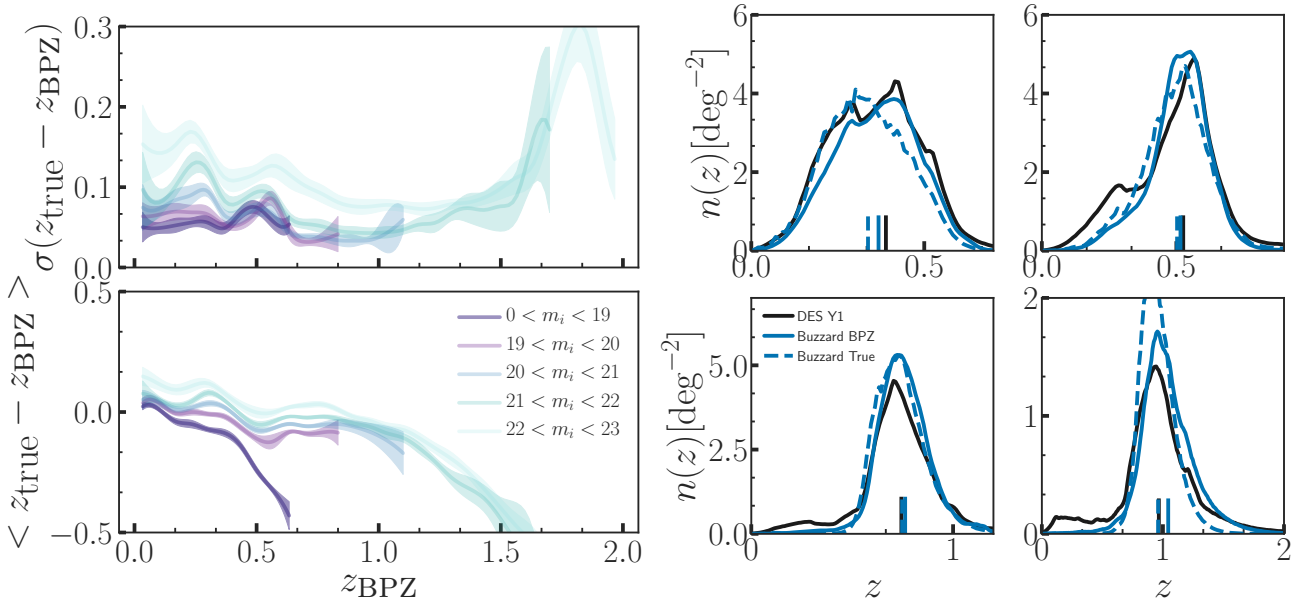


Figure 7. Photometric redshift performance. Left: Scatter and bias of BPZ photo- z estimates as a function of redshift and magnitude for the simulated 'gold' galaxy sample. We do not attempt to compare this particular measurement to data, due to the lack of a complete spectroscopic validation set in the data. Right: The redshift distribution of the Buzzard METACALIBRATION sample in the four source bins, ranging from low to high redshift from right to left and top to bottom, used for the Y1 3×2 point analysis. These are estimated by stacking random draws from $p(z)$ as determined by BPZ (solid blue), and from true redshifts (dashed blue) compared to the $n(z)$ estimated for the DES Y1 METACALIBRATION sample by stacking random draws from $p(z)$ as determined by BPZ (black). Vertical lines represent the means of each of these distributions.

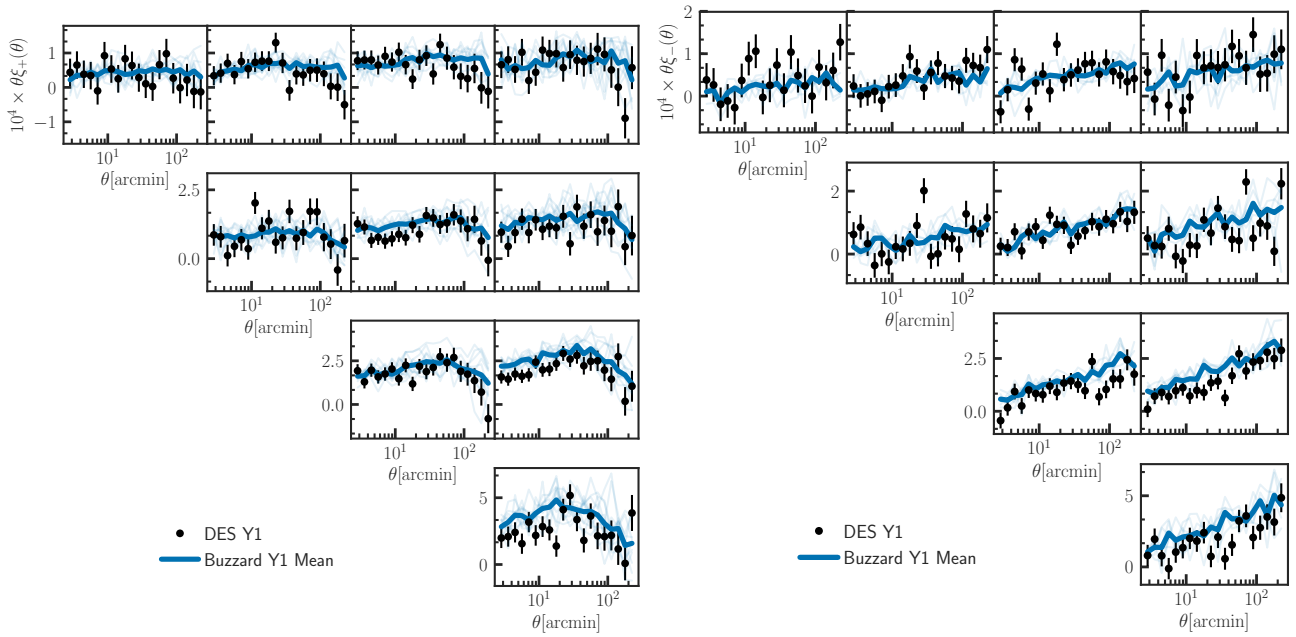


Figure 8. Comparison of $\xi_{+/-}$ tomographic auto- and cross correlations between the mean of all Buzzard simulations (solid blue) and DES Y1 (black). Light blue lines are measurements from individual simulations. The different panels the unique cross-correlations between tomographic bins, where tomographic bins go from low to high redshift from left to right and top to bottom.

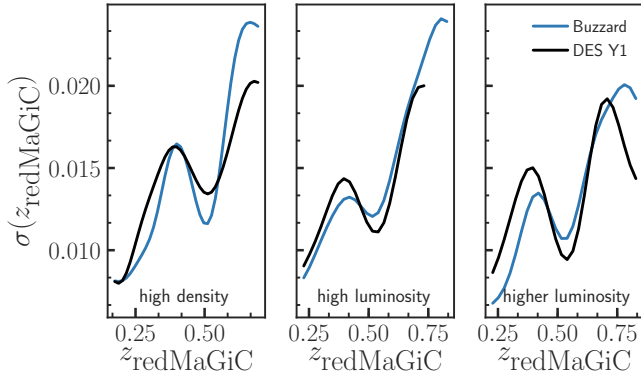


Figure 9. Comparison of REDMAGIC photo- z s between Buzzard (blue) and DES Y1 (black). The three columns are the REDMAGIC high density, high luminosity and higher luminosity samples from left to right. The figure shows the estimation of the photo- z errors as reported by the REDMAGIC algorithm.

4.2. redMaGiC

We also apply the REDMAGIC selection algorithm to our simulations. In this case, unlike for the METACALIBRATION sample, it is possible for us to use the same selection algorithm in the simulations as is used in the data.

The REDMAGIC galaxy sample was used extensively in the DES Y1 cosmology analyses as a sample with robust photometric redshifts. As such we would like to validate that our simulations reproduce this performance. As discussed in Sec. 4.3, the ADDGALS algorithm produces a red sequence very similar to that found in the data, and thus the scatter of the REDMAGIC photo- z s is also similar as can be seen in Fig. 9. Here we cite $\sigma(z_{redmagic})$ as the mean of the internal REDMAGIC estimate of this quantity in bins of $z_{redmagic}$. REDMAGIC determines this quantity for each galaxy from a combination of the width of the red sequence, photometric errors on that galaxy, and an after-burner calibration on REDMAPPER photometric redshifts. We find that $\sigma(z_{redmagic})$ in Buzzard is slightly smaller than its counterpart in the DES Y1 data at low redshift and slightly higher at high redshift. The level of discrepancy between the simulations and the data in this metric has yet to pose significant issues to DES analyses using these simulations. As measurements become more precise, the underestimates of photo- z errors here could lead to over-optimism in systematics estimation using Buzzard.

We also wish to compare our simulated REDMAGIC sample to the data at the level of the statistics used for the DES Y1 cosmology analyses, namely angular clustering, $w(\theta)$, and galaxy-galaxy lensing, $\gamma_t(\theta)$. We refer the reader interested in the details of these measurements to MacCrann et al. (2018) and DES Collaboration et al. (2017). In Fig. 10 we compare the mean value of $w(\theta)$ over our 18 simulated samples with the data in the five lens redshift bins that were used

in the DES Y1 clustering data vector. The first three bins use the high density REDMAGIC sample, the fourth uses the high luminosity REDMAGIC sample and the higher luminosity sample is used in the fifth bin. Because the REDMAGIC photo- z performance in the simulations closely matches what is found in the data, differences in clustering here can be interpreted as differences in the (non-linear) bias of our simulations and the real universe. In the first, second, third and fifth redshift bins the match between the simulations and the data is good. In the fourth bin, the simulations have an excess of clustering with respect to what is found in the data. While a large number of REDMAGIC galaxies are placed in unresolved halos in our simulations, given that this sample is thought to populate halos down to masses of approximately $M_{vir} \approx 10^{12} h^{-1} M_{\odot}$, it is unlikely that the discrepancies between our simulations and the data as seen here are due to resolution effects given the resilience of the ADDGALS method to resolution for large-scale clustering as demonstrated in Wechsler et al. (2019). Instead, we observe that the REDMAGIC sample in our simulations in the fourth bin is somewhat brighter than that observed in the data, giving a plausible explanation for the higher values of bias, given that brighter galaxies are in general more clustered.

Additional tests have shown that above $10 h^{-1} \text{Mpc}$ the bias of the REDMAGIC sample in the simulations conforms to a linear bias model. Discrepancies such as those exhibited here may be relevant when estimating the impact of effects such as non-linear bias on various analyses, thus these simulations should not be used to *prove* that any given analysis is immune to such systematics. Rather, the Buzzard simulations represent a plausible testing ground in which to perform necessary but not sufficient tests of the efficacy of an analysis. We also present measurements of γ_t in Fig. 10, where we only show lens-source combinations with the sources behind the lenses, and we have not included the 5th lens bin for clarity of presentation. Again, the data and simulations are in good agreement.

These comparisons demonstrate that our simulated REDMAGIC sample does indeed resemble the sample as selected in the data. This is a non-trivial success of these simulations as this level of agreement requires matches between nearly every aspect of our simulations, including colors, luminosities, and galaxy-halo connection, and the data. Although we have shown that there are some quantitative discrepancies between the simulations and the data, these tests show that this sample can be used as a realistic proxy for data when developing and validating algorithms using the REDMAGIC sample.

4.3. redMaPPer

The low computational cost of the pipeline outlined in this work also makes it ideal for use in the study of photomet-

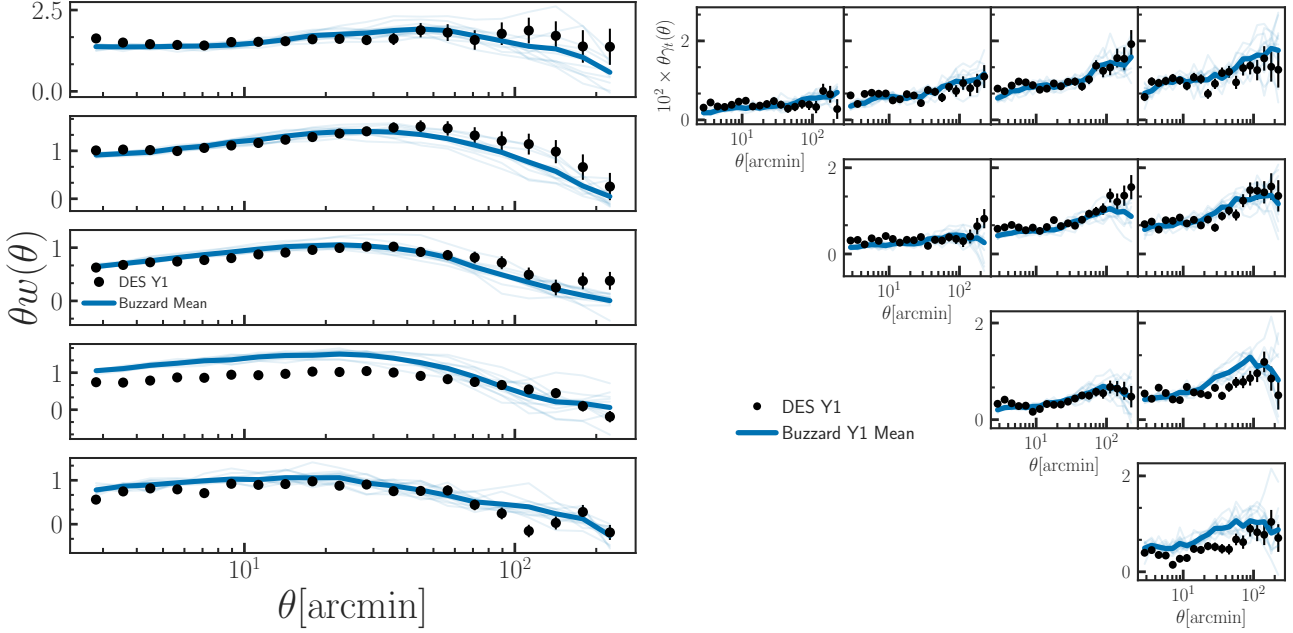


Figure 10. Left: Comparison of redMaGiC sample clustering between Buzzard and DES Y1. Top to bottom is low to high redshift with bins of 0.15-0.3, 0.3-0.45, 0.45-0.6, 0.6-0.75, 0.75-0.9. Right: Comparison of galaxy–galaxy lensing around redMaGiC sample between Buzzard and DES Y1 for all lens–source configurations with lenses in front of sources, using only the first 4 lens bins for readability.

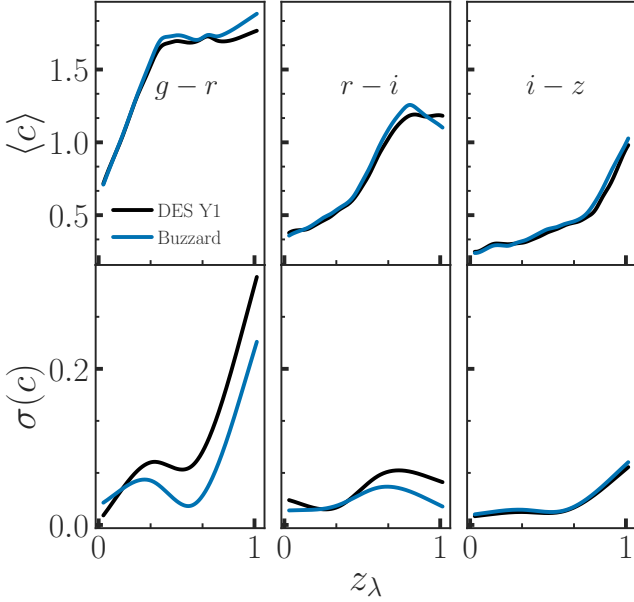


Figure 11. A comparison of the mean and scatter of red-sequence galaxy colors between Buzzard and DES Y1 redMaPPer samples.

rically identified cluster catalogs, where very large-volume simulations are required to match the statistics in the data. In order to facilitate these studies, we have run the REDMAPPER cluster finder on our simulations using the same configuration as used in the DES Y1 data.

In order to produce simulated cluster catalogs whose properties match the data, a number of observables must be re-

produced at high fidelity. Firstly, a tight red sequence must be present in the simulated galaxies’ color distribution. Our method for populating simulations with SEDs produces realistic color distributions, especially for quenched galaxies whose rest-frame SEDs do not seem to evolve much with redshift from their low redshift counterparts. This allows us to reproduce the galaxy red sequence to high fidelity, as seen in Fig. 11. At high redshift the scatter in the red sequence of the data appears larger than that observed in the simulations, especially in $g-r$. One possible explanation for this is that our SEDs are constrained best in the rest-frame optical, where the SEDs of the SDSS spectroscopic sample used for our training set are measured. At high redshift, the g and r bands are measuring the rest frame UV, and as such there is the possibility for significant deviations of these bands from what is predicted from our training set.

In addition to running REDMAPPER with the standard configuration used on the data, we have also produced a catalog that uses the same red sequence model, but measures richnesses around the true halo centers in our simulations. By doing this we can learn about the $\lambda-M_{200b}$ relationship without the complications imparted by mis-centering due to structures projected along the line-of-sight. In Fig. 12, we present a comparison of the measured $\lambda-M_{200b}$ relation using true halo centers with that inferred using the DES Y1 data (McClintock et al. 2018). We see a deficit in richness at fixed mass when compared to the DES Y1 measurements. This is due to the inability of our model to perfectly reproduce quenched galaxy clustering, leading to fewer red satel-

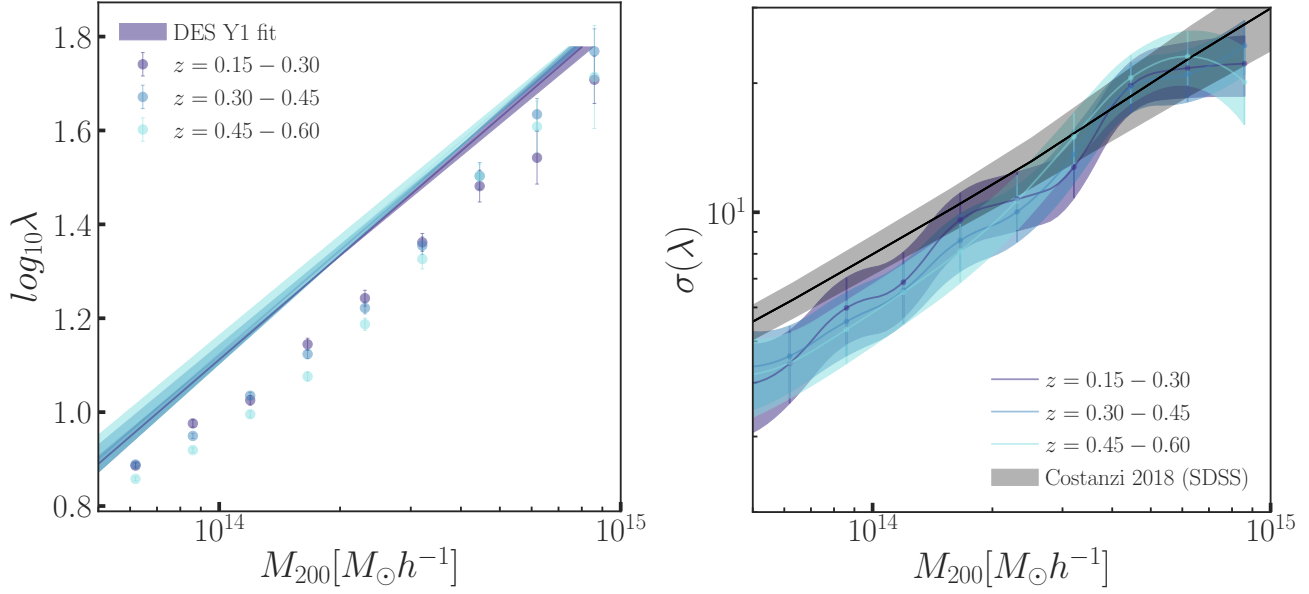


Figure 12. redMaPPer mass- λ relationship. *Left:* The mass–richness relation in Buzzard compared to that inferred in DES Y1 redMaPPer clusters. The model fits to the data are the solid lines, the simulations are the points with error bars given by the error on the mean. *Right:* Intrinsic scatter in the Buzzard mass–richness relation as a function of redshift compared to low redshift constraints from SDSS (Costanzi et al. 2019). Lines between simulation measurements are quadratic interpolations.

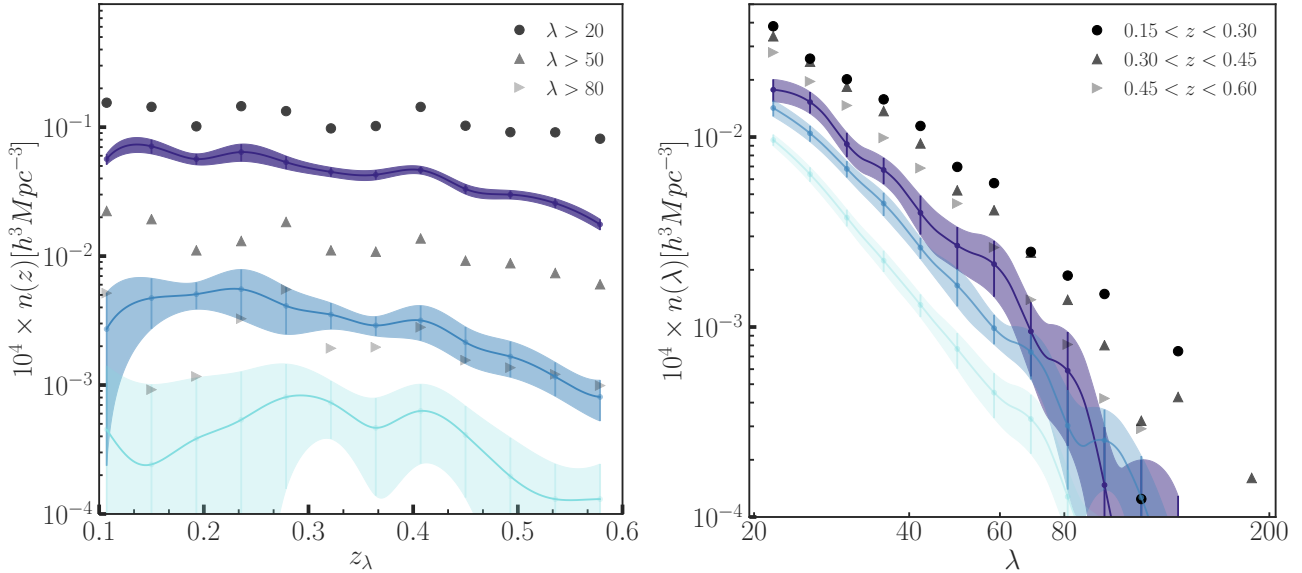


Figure 13. redMaPPer λ abundance function. *Left:* The number of REDMAPPER identified clusters for a few richness cuts as a function of redshift in Buzzard (lines) compared to the DES Y1 data (black points). Higher transparency points represent higher richness measurements. *Right:* Counts of the number of REDMAPPER identified clusters in Buzzard (lines) compared to the DES Y1 data (black points) as a function of richness in three different redshift bins. Higher transparency points represent higher redshift measurements.

lite galaxies in massive halos than found in the data (Wechsler et al. 2019).

In the right hand panel, we show measurements of the scatter in the $\lambda_{obs} - M_{200b}$ relation in our simulations. The DES weak-lensing cluster mass calibration presented in McClintock et al. (2018) does not constrain the scatter in this relation, so we cannot compare explicitly to DES data, but these values for scatter are consistent with those presented in other REDMAPPER analyses, such as Costanzi et al. (2019) (shown in black), showing a marginal preference for lower scatter at low halo masses than what is found in the data.

In Fig. 13 we present a comparison between the mean number densities of the 18 simulated redMaPPer catalogs and the data as a function of redshift and cluster richness, λ . For these comparisons, we use REDMAPPER catalogs run with the same configuration used on the data. The simulations under-predict the data number densities with the discrepancy becoming worse at high redshift. This is consistent with the under-prediction of richness at fixed halo mass as observed in Fig. 12. This is likely additionally exacerbated by marginally lower scatter in richness at fixed mass in our simulations compared to the data. Aside from the observed discrepancy between number densities of clusters in the data and our simulations, the redshift evolution of these quantities is in the same direction, with the simulations showing more redshift evolution at high redshift than the data.

Overall, the simulations presented here have more difficulty matching REDMAPPER observables compared to the other samples presented in this work due to their sensitivity to the spatial dependence of galaxy colors down to small scales. Future improvements to these simulations aimed at improving these observables will focus on new methods for assigning galaxy SEDs to their correct locations in the cosmic web and for using larger samples of data to constrain one-point statistics such as the luminosity functions and f_{red} so that rare galaxy populations such as cluster members are sampled with higher statistics. Nonetheless, these simulations represent the state of the art in reproducing the cluster observables shown here. We are currently using these simulations to test aspects of the DES cluster cosmology analysis. These simulations should not be used to calibrate analyses, but the qualitative agreement between the observables presented here demonstrates that they can be used as a plausible simulated universe on which to test analysis pipelines and develop algorithms.

5. SUMMARY

This paper presents a suite of 18 synthetic DES Y1 catalogs out to $z = 2.35$ and to a depth of $r \sim 26$ (excluding very bright objects at $z > 2.35$). They include:

- halo and particle catalogs
- galaxy positions, magnitudes, ellipticities, and sizes

- lensing for each galaxy via a curved sky ray-tracing algorithm
- realistic photometric errors, masking and photometric redshifts
- REDMAGIC, REDMAPPER, and weak-lensing source samples

We have demonstrated the fidelity of these catalogs by comparing relevant observables to data or theory where applicable, with a focus on those tests that are most relevant for the cosmological analysis of current DES data:

- matter power spectra, halo mass functions and halo bias
- galaxy magnitude and color distributions
- photometric redshift distributions
- 3×2 point observables in the DES Y1 lens and source bins
- REDMAPPER mass-observable relation and number densities

This provides a high-fidelity reproduction of the DES Y1 data that facilitates study of many large-scale structure probes simultaneously, including galaxy clustering, optically selected galaxy clusters, shear correlation functions, and the lensing profiles of galaxies and clusters.

The limiting factors in the fidelity of these simulations are twofold. The first limitation is our methodology for tuning the free parameters of our galaxy model. Ideally, one would optimize these parameters jointly by tuning to the observations that we wish to reproduce, e.g. DES 3x2-point observables and cluster abundances, via an iterative optimization scheme. This is currently infeasible, as the pipeline beginning with our galaxy model and including necessary observational effects such as ray-tracing, photometric errors, photometric redshift estimation and sample selection, takes much too long to run such an optimization algorithm on. Instead we have settled for tuning these parameters individually, sometimes by hand, e.g. in the case of the red-fraction of galaxies. Progress in optimizing the parameters of ADDGALS may either be made by constructing fast proxies for the relevant observables as a function of our model parameters, or by simply speeding up the process of running each simulation.

The second limitation is the simplifying assumptions that we have made to extrapolate our model to high redshift. This is manifest in a few ways, in particular the discrepancies between the colors in Buzzard and COSMOS at high redshift as detailed in Sec. E.2, and discrepancies with the data in observed magnitude distributions (Sec. E.1) and clustering (Sec. 4.2). Progress here will necessitate updates to

galaxy models, in particular the SEDs that we use at high redshift and our parameterization of the galaxy–halo connection. These upgrades are already underway.

The strategy we pursued here was designed to work with moderate resolution simulations that can be run on relatively standard clusters today. The rough computation time from initial conditions to a final catalog is $\sim 150,000$ CPU hours, and we can complete this end-to-end pipeline in approximately one week. It has already allowed the efficient production of many times the DES volume, which has proven essential for developing realistic error estimates from surveys. This strategy will also allow us to repeat the catalog creation a number of times with differing choices of the cosmological model, the galaxy evolution model, and the model for inclusion of systematic errors.

There are however significant scientific motivations for higher resolution simulations, which allow for more accurate models of the galaxy–halo connection. Ideally, one would model the entire galaxy population presented here in simulations that resolve galactic substructures (for example, see the low redshift synthetic galaxy distribution presented in [Reddick et al. 2013](#)). In [Wechsler et al. \(2019\)](#), we have reviewed the computing challenges that must be overcome to achieve this and the limitations of the specific resolution choice made here. We emphasize that the pipeline we have developed here is modular, and can be readily extended, including to higher resolution simulations.

Upon posting of this article we are making the simulations described here available upon request. This includes the underlying N -body simulations, the 10,313 square degree galaxy catalogs, as well as the METACALIBRATION, REDMAGIC, and REDMAPPER catalogs, random points, and the 3×2 point data vectors presented in this paper.

We will make the aforementioned data products freely downloadable at [BuzzardFlock.github.io](https://github.com/BuzzardFlock) at the time this study and its companion papers are published⁹. We expect that this can be of use in a wide range of studies of large-scale structure, galaxy clusters, weak lensing, and photometric redshift distributions.

We are very grateful to numerous Dark Energy Survey collaborators who provided useful tests of these catalogs during various stages of development. These include Joanne Cohn, Chihway Chang, Joerg Dietrich, Tim Eifler, Oliver Friedrich, Daniel Gruen, Jiangang Hao, Elisabeth Krause, Boris Leistedt, Eduardo Rozo, Eusebio Sanchez, Michael Troxel, Martin White, and Yuanyuan Zhang.

Some of the computing for this project was performed on the Sherlock cluster. We would like to thank Stanford University and the Stanford Research Computing Center for providing computational resources and support that contributed to these research results. This research used resources of the National Energy Research Scientific Computing Center (NERSC), a U.S. Department of Energy Office of Science User Facility operated under Contract No. DE-AC02-05CH11231. Some of the cosmological simulations were also run on the XSEDE machine Ranger. This work was completed in part with resources provided by the University of Chicago Research Computing Center. We are grateful to Stuart Marshall and the rest of the SLAC computing team for extensive support of this work. Application support was provided by the Advanced Support for TeraGrid Applications. We thank Volker Springel for providing the L-Gadget2 code.

JD, RHW, MB, MRB received support from the U.S. Department of Energy under contract number DE-AC02-76SF00515, including support from a SLAC LDRD grant, and from a Terman Fellowship at Stanford University. MECS was supported by the NSF under Award No. AST-0901965. Argonne National Laboratory’s work was supported by the U.S. Department of Energy, Office of Science, Office of Nuclear Physics, under contract DE-AC02-06CH11357.

This study made use of the SDSS DR7 Archive, for which funding has been provided by the Alfred P. Sloan Foundation, the Participating Institutions, the National Aeronautics and Space Administration, the National Science Foundation, the U.S. Department of Energy, the Japanese Monbukagakusho, and the Max Planck Society. The SDSS Web site is <http://www.sdss.org/>. The SDSS is managed by the Astrophysical Research Consortium (ARC) for the Participating Institutions: the University of Chicago, Fermilab, the Institute for Advanced Study, the Japan Participation Group, the Johns Hopkins University, Los Alamos National Laboratory, the Max-Planck-Institute for Astronomy (MPIA), the Max-Planck-Institute for Astrophysics (MPA), New Mexico State University, University of Pittsburgh, Princeton University, the United States Naval Observatory, and the University of Washington.

Funding for the DES Projects has been provided by the U.S. Department of Energy, the U.S. National Science Foundation, the Ministry of Science and Education of Spain, the Science and Technology Facilities Council of the United Kingdom, the Higher Education Funding Council for England, the National Center for Supercomputing Applications at the University of Illinois at Urbana-Champaign, the Kavli Institute of Cosmological Physics at the University of Chicago, the Center for Cosmology and Astro-Particle Physics at the Ohio State University, the Mitchell Institute for Fundamental Physics and Astronomy at Texas A&M University, Financiadora de Estudos e Projetos, Fundação

⁹ Interested users of the catalog before this time are encouraged to contact the authors at jderose@stanford.edu or rwechsler@stanford.edu

Carlos Chagas Filho de Amparo à Pesquisa do Estado do Rio de Janeiro, Conselho Nacional de Desenvolvimento Científico e Tecnológico and the Ministério da Ciência, Tecnologia e Inovação, the Deutsche Forschungsgemeinschaft and the Collaborating Institutions in the Dark Energy Survey.

The Collaborating Institutions are Argonne National Laboratory, the University of California at Santa Cruz, the University of Cambridge, Centro de Investigaciones Energéticas, Medioambientales y Tecnológicas-Madrid, the University of Chicago, University College London, the DES-Brazil Consortium, the University of Edinburgh, the Eidgenössische Technische Hochschule (ETH) Zürich, Fermi National Accelerator Laboratory, the University of Illinois at Urbana-Champaign, the Institut de Ciències de l’Espai (IEEC/CSIC), the Institut de Física d’Altes Energies, Lawrence Berkeley National Laboratory, the Ludwig-Maximilians Universität München and the associated Excellence Cluster Universe, the University of Michigan, the National Optical Astronomy Observatory, the University of Nottingham, The Ohio State University, the University of Pennsylvania, the University of Portsmouth, SLAC National Accelerator Laboratory, Stanford University, the University of Sussex, Texas A&M University, and the OzDES Membership Consortium.

Based in part on observations at Cerro Tololo Inter-American Observatory, National Optical Astronomy Observatory, which is operated by the Association of Universities for Research in Astronomy (AURA) under a cooperative agreement with the National Science Foundation.

The DES data management system is supported by the National Science Foundation under Grant Numbers AST-1138766 and AST-1536171. The DES participants from Spanish institutions are partially supported by MINECO under grants AYA2015-71825, ESP2015-66861, FPA2015-68048, SEV-2016-0588, SEV-2016-0597, and MDM-2015-0509, some of which include ERDF funds from the European Union. IFAE is partially funded by the CERCA program of the Generalitat de Catalunya. Research leading to these results has received funding from the European Research Council under the European Union’s Seventh Framework Program (FP7/2007-2013) including ERC grant agreements 240672, 291329, and 306478. We acknowledge support from the Australian Research Council Centre of Excellence for All-sky Astrophysics (CAASTRO), through project number CE110001020, and the Brazilian Instituto Nacional de Ciência e Tecnologia (INCT) e-Universe (CNPq grant 465376/2014-2).

This manuscript has been authored by Fermi Research Alliance, LLC under Contract No. DE-AC02-07CH11359 with the U.S. Department of Energy, Office of Science, Office of High Energy Physics. The United States Government retains and the publisher, by accepting the article for publication, acknowledges that the United States Government retains a non-exclusive, paid-up, irrevocable, world-wide license to publish or reproduce the published form of this manuscript, or allow others to do so, for United States Government purposes.

APPENDIX

A. MODELED GALAXY PROPERTIES IN THE FINAL CATALOG

A list of modeled intrinsic and observed galaxy properties as well as halo properties included in the data release are provided in Tables 2-4. Parameters related to halo ellipticities and angular momenta are determined using all particles within R_{vir} . For more information about the released data including file formats and data access instructions, please see [BuzzardFlock.github.io](https://github.com/BuzzardFlock).

B. *N*-BODY SIMULATION METHODOLOGY

B.1. *Lightcone Simulations*

To model large photometric surveys it is necessary to create a dark matter particle distribution built on a lightcone. We create the lightcones on the fly as the simulation runs. Here, every time a particle is moved during the drift step of the leap-frog integrator, we check to see if it crosses the light cone surface $r(a)$ — the comoving distance from the origin of the light cone, r , at the time of the simulation scale factor, a . If a particle on the previous time step is inside the light cone surface of the previous time step and then is outside the light cone surface of the current time step, then it has crossed the light cone surface. Specifically, for particle i with comoving distances from the light cone origin on the previous time step $n-1$, $r_{n-1}^{(i)}$ and similarly for the current time step n , $r_n^{(i)}$, we check that

$$r_{n-1}^{(i)} < r(a_{n-1}) \quad \text{and} \quad r_n^{(i)} \geq r(a_n)$$

where the scale factor of time step n is a_n . If a particle satisfies the light cone crossing condition, we use an interpolation to find the intersection of the particle’s trajectory with the light cone surface. For each particle, consider its positions on two consecutive time steps x_n and x_{n+1} . As in [Evrard et al. \(2002\)](#), we define an interpolation parameter α such that

Name	Description	Unit
ID	A unique identification number for each object.	N/A
TRA	Simulated right ascension (unlensed).	degrees
TDEC	Simulated declination (unlensed).	degrees
Z_COS	Redshift (only including Hubble flow)	N/A
AMAG	Galaxy absolute magnitude in DES grizY bands in $z=0.1$ frame	$h^{-1}\text{mag}$
TMAG	True apparent galaxy magnitudes in grizY bands	mag
MAG_R	SDSS r -band absolute magnitude in $z=0.1$ frame.	$h^{-1}\text{mag}$
P [XYZ]	3D comoving galaxy positions	$h^{-1}\text{Mpc}$
V [XYZ]	3D physical velocity	$s^{-1}\text{km}$
TE	Ellipticity in local RA and DEC directions	N/A
TSIZE	Galaxy half-light radius	arcsec
GAMMA1	Weak lensing shear in the local RA direction	N/A
GAMMA2	Weak lensing shear in the local DEC direction	N/A
KAPPA	Weak lensing convergence	N/A
MU	Weak lensing magnification	N/A
SEDID	Index of SDSS galaxy from SED training set	N/A
COEFFS	Coefficients of SED template from KCORRECT	N/A
HALOID	ID of halo nearest to the galaxy in 3D	N/A
M200	Halo mass (M200B) of the halo nearest to the galaxy in 3D	$h^{-1}M_{\odot}$
R200	Comoving radius of the halo nearest to the galaxy in 3D corresponding to M200B	$h^{-1}\text{Mpc}$
RHALO	Distance to the nearest halo in 3D $h^{-1}\text{Mpc}$	$h^{-1}\text{Mpc}$
CENTRAL	A flag indicating if the galaxy is the central galaxy of a resolved halo.	N/A

Table 2. Intrinsic Galaxy Properties

Name	Description	Unit
Z	Redshift (including redshift space distortions)	N/A
RA	Lensed right ascension	N/A
DEC	Lensed declination	N/A
LMAG	Lensed apparent galaxy magnitude in DES grizY bands	mag
MAG_[GRIZ]	Noisy lensed apparent galaxy magnitude in DES grizY bands	mag
MAGERR_[GRIZ]	Galaxy magnitude errors in DES grizY bands	mag
FLUX_[GRIZ]	Noisy lensed galaxy fluxes in DES grizY bands	nanomaggies
IVAR_[GRIZ]	Inverse variance of galaxy fluxes in DES grizY bands	nanomaggies ⁻²
EPISLON	Lensed ellipticity in local RA and DEC directions	N/A
SIZE	Lensed galaxy half-light radius	arcmin
Z_MEAN	Mean redshift estimate as determined by BPZ	N/A
Z_MC	Monte Carlo draw from BPZ $p(z)$	N/A

Table 3. Observed Galaxy Properties

Name	Description	Unit
HALOID	A unique identification number for each halo	N/A
RA	Lensed right ascension	degrees
DEC	Lensed declination	degrees
TRA	Unlensed right ascension	degrees
TDEC	Unlensed declination	degrees
Z	Redshift including redshift space distortions	N/A
Z_COS	Redshift including only Hubble flow	N/A
M200	Halo mass, $M_{200,\text{background}}$	$h^{-1}M_{\odot}$
R200	Comoving halo radius, $R_{200,\text{background}}$	$h^{-1}\text{Mpc}$
M200C	Halo mass, $M_{200,\text{crit}}$	$h^{-1}M_{\odot}$
R200C	Comoving halo radius, $R_{200,\text{crit}}$	$h^{-1}\text{Mpc}$
M500C	Halo mass, $M_{500,\text{crit}}$	$h^{-1}M_{\odot}$
R500C	Comoving halo radius, $R_{500,\text{crit}}$	$h^{-1}\text{Mpc}$
MVIR	Halo mass, M_{vir}	$h^{-1}M_{\odot}$
RVIR	Comoving halo radius, R_{vir}	$h^{-1}\text{Mpc}$
M2500	Halo mass, $M_{2500,\text{crit}}$	$h^{-1}M_{\odot}$
R2500	Comoving halo radius, $R_{2500,\text{crit}}$	$h^{-1}\text{Mpc}$
VRMS	3D velocity dispersion of particles in the halo within R_{vir}	$s^{-1}\text{km}$
RS	Comoving halo scale radius from NFW profile fit	$h^{-1}\text{kpc}$
J[X, Y, Z]	Halo angular momentum	$(h^{-1}M_{\odot})(h^{-1}\text{Mpc}) s^{-1}\text{km}$
LAMBDA	Halo spin parameter	N/A
HALO[PX, PY, PZ]	Comoving 3D halo position	$h^{-1}\text{Mpc}$
HALO[VX, VY, VZ]	Physical 3D peculiar halo velocity	$s^{-1}\text{km}$
HOST_HALOID	HALOID of the host halo for subhalos, set to HALOID of the halo for central halos	N/A
XOFF	Comoving 3D offset of density peak from average particle position	$h^{-1}\text{kpc}$
VOFF	Physical 3D offset of density peak from average particle velocity	$s^{-1}\text{km}$
B_TO_A	Ratio of second to first largest halo ellipsoid axis	N/A
C_TO_A	Ratio of third to first largest halo ellipsoid axis	N/A
A[X, Y, Z]	Direction of the major axis of the halo ellipsoid	N/A

Table 4. Halo properties

$$x_{\alpha} = x_n + \alpha v_n dt,$$

where $x_{n+1} = x_n + v_n dt$, dt is the time step, and v_n is the velocity at time step n . L-Gadget2 uses a leap-frog integrator and thus this the velocity is formally displaced by half a time step behind the position. We label it at the same time step for simplicity. The light-cone crossing tests and interpolation are done during the drift step of the leap-frog integrator, so that as α ranges from zero to one, it traces exactly the particle's trajectory.

When the particle crosses the light cone surface, it satisfies the following condition

$$|x_{\alpha}|^2 = r^2(t_n + \alpha dt),$$

with t_n being the time at time step n . To define the interpolation, at each time step we compute once an approximation to the function $r^2(t_n + dt\alpha)$ defined as

$$r^2(t_n + \alpha dt) \approx a\alpha^2 + b\alpha + c .$$

In our implementation, this approximation is computed through a least-squares fit of tabulated squared comoving distances which span the range of the time step dt . We enforce the conditions that at $\alpha = 0$ and $\alpha = 1$ the fit produce the correct comoving distances. Thus there is only one free parameter in the fit for which the least-squares fit is a simple average, making this procedure extremely efficient. Because the comoving distance as a function of α is quite smooth, the slight increase in expense incurred by computing and using the expansion above is offset by a substantial increase in the accuracy of the interpolation.

With this approximation in hand, the intersection of the particle with the light cone surface can be computed quickly by solving a quadratic equation

$$(dt^2|v_n|^2 - a)\alpha^2 + (2dt v_n \cdot x_n - b)\alpha + |x_n|^2 - c = 0$$

and selecting the appropriate root. To compute the scale factor at the particle's intersection with the light cone surface, we use a tabulated set of $\{t_i, a_i\}$ values to find a_α given $t_\alpha = t_n + \alpha dt$. We can use this scale factor to test the light cone intersection criterion, $|x_\alpha|^2 = r^2(a_\alpha)$. We find that this condition is satisfied to $\lesssim 1 h^{-1} \text{kpc}$.

During the light cone construction, we consider a single fiducial observer at $(0,0,0)$ in the domain of the simulation cube with length L . We create an entire 4π steradians of light cone coverage using the periodicity of the simulation volume to translate the particles into each of the eight cubes which intersect the $(0,0,0)$ point in the lattice of simulation cubes. We test for light cone crossing in each of these eight cubes to generate eight octants which cover the entire sky. In practice an extra layer of cubes beyond this fiducial eight is used to catch extra particles around the corners of the fiducial eight cubes. This extra layer is discarded once the light cone surface has moved sufficiently into the interior of the volume of the eight fiducial cubes. Particles can be output twice into the same octant at different scale factors in this scheme. Our procedure ensures that the large-scale structure is continuous between the different octants of the light cone. Additionally, by choosing carefully which particles to save, we can generate pencil-beam light cones of different geometries if desired.

The procedure described above generates a full-sky light cone out to comoving distance L for a simulation with side length L . This full sky light cone has repetitions out to comoving distance L , but encloses a unique simulation volume out to a comoving distance of $L/2$, and any given octant is unique out to a distance of L . The full sky light cone is used for the weak-lensing ray tracing calculations as described below to achieve the proper boundary conditions.

B.2. High-Resolution Tuning Simulation

We run a single higher-resolution simulation used to tune the ADDGALS galaxy assignment algorithm. For this, we require a simulation with sufficient resolution to use the subhalo abundance matching technique (SHAM; see e.g. Conroy et al. 2006b; Reddick et al. 2013) to model the galaxy distribution down to roughly $M_r = -19$. To do this we use a simulation box of size $400 h^{-1} \text{Mpc}$ with 2048^3 particles. At this resolution, the SHAM catalog is not strictly complete down to -19 , as subhalos near the cores of massive hosts are stripped below the simulation resolution (see Reddick et al. 2013 for a detailed discussion). However, comparisons with SDSS data show that the resolution is sufficient to model the observed 2-point function to $r_p \sim 300 h^{-1} \text{kpc}$ to within current observational errors down to $M_r = -19$, and moderately well below this limit Wechsler et al. (2019). A lightcone output is not necessary for this computational volume, but we require merger trees to construct the abundance matching catalog. For this, we save 100 simulation snapshots logarithmically spaced from $z = 12$ to $z = 0$, which allows construction of accurate merger trees.

B.3. Halo Finding

Halo finding is done with the publicly available adaptive phase-space halo finder ROCKSTAR¹⁰ (Behroozi et al. 2013a). ROCKSTAR is very efficient and accurate (see for example, the halo finder comparison in Knebe et al. 2011). It is particularly robust in galaxy mergers, important for the massive end of the halo mass function, and in tracking substructures, important for the abundance matching procedure applied to the tuning simulation. The total number of halos with more than 100 particles found in the lightcone volume used for each simulation is given in Table 1. We have chosen to use M_{vir} strict spherical overdensity (SO) masses (Bryan & Norman 1998); additional halo mass definitions are output by ROCKSTAR using these centers. ROCKSTAR also

¹⁰ <https://bitbucket.org/gfcstanford/rockstar>

outputs several other halo properties, including other halo mass measurements, concentration, shape, and angular momentum (see Behroozi et al. 2013a, for details).

Comparisons between our simulations and standard halo mass function (McClintock et al. 2018) and halo bias (Tinker et al. 2010) models are shown in Fig. 2. In both cases measurements are averaged over 3 sets of 10,313 square degree simulations and the error bars plotted are the error on the mean estimated via jackknife. The mass functions in L1 (measured for $0.0 < z \leq 0.34$) and L2 (measured for $0.34 < z \leq 0.9$) agree very well with McClintock et al. (2018), with discrepancies at low mass likely due to differences in halo finding, as the simulations used in McClintock et al. (2018) identified halos using strict spherical overdensity estimates around centers defined using M_{200b} rather than re-measuring M_{200b} around centers defined when finding halos using M_{vir} as the halo definition in this work. The mass functions in L3 deviate from the emulator prediction in a mass dependent way that is likely attributable to the low mass resolution in these simulations. The right panel of Fig. 2 shows halo bias measurements for a bin of mean mass equal to $4 \times 10^{13} h^{-1} M_{\odot}$ in the L1 ($z = 0.26$), L2 ($z = 0.54$) and L3 ($z = 1.34$) simulations compared to the Tinker et al. (2010) bias model. These measurements as well as measurements we performed at higher masses and different redshifts agree to within the quoted 6% error on the model.

B.4. Merger Tree

For the highest resolution “tuning simulation”, we track the formation of halos using 100 saved snapshots between $z = 12.3$ and $z = 0$, equally spaced in $\Delta \ln a$. The gravitationally-consistent merger tree algorithm¹¹ described in Behroozi et al. (2013b) is applied to track halos. This algorithm explicitly checks for consistency in the gravitational evolution of dark matter halos between time steps, and leads to very robust tracking. Details of the implementation and its robustness can be found in Behroozi et al. (2013b). Using the resulting merger trees, we are able to track v_{max} and v_{vir} at M_{peak} for each identified subhalo. The quantity

$$v_{\alpha} = \left(\frac{v_{\text{max}}}{v_{\text{vir}}} \right)^{\alpha} \quad (\text{B1})$$

with $\alpha = 0.68$ is used to assign galaxies to dark matter halos, using an abundance matching algorithm described by Lehmann et al. (2017) with 0.17 dex scatter in absolute magnitude.

C. WEAK GRAVITATIONAL LENSING IMPLEMENTATION

We calculate the shear and magnification applied to the galaxy by weak gravitational lensing. To do this calculation, we use the multiple-plane ray tracing code CALCLENS described in Becker (2013). With a multiple-plane ray tracing code, we can correctly find the lensed images of the galaxies (including multiply imaged objects) and we naturally include higher-order corrections to the Born approximation in the shear and convergence fields (e.g., Hilbert et al. 2009). Multiple-plane ray tracing codes use the Limber approximation to relate the surface mass density in radial shells along the line-of-sight of the light cone to the lensing potential in each shell through a two-dimensional Poisson equation (e.g., Jain et al. 2000). Once this two-dimensional Poisson equation is solved, the derivatives of the lensing potential are then used to propagate the ray locations and their inverse magnification matrices shell to shell from the observer to the furthest edge of the light cone.

The multiple-plane ray tracing code CALCLENS of Becker (2013) tracks both the ray positions and the inverse magnification matrix at each ray, correctly accounts for the sky curvature in the Limber approximation, uses HEALPIX¹² (Górski et al. 2005) for the ray locations to achieve uniform resolution over the sphere, and finds the galaxy images using a grid search algorithm (e.g., Schneider et al. 1992; Hilbert et al. 2009; Fosalba et al. 2008) implemented on the sphere. A grid search algorithm is capable of correctly finding multiple images of the same source. However, the lens causing the multiple images must be properly resolved in order for these multiple images to be correct. Thus given the resolution of the simulations used in this work, in practice very few multiple images are found for a given source galaxy catalog and those that are found are not expected to be computed accurately. Also, as implemented currently, only the average position of the multiple images is computed, so that strong lensing features like arcs are not captured in the catalogs. While CALCLENS has the capability to use a combination SHT+Multigrid Poisson solver for the sphere, for this work we choose to use just the SHT version as it is slightly more accurate. Once the inverse magnification matrix and lensed position of each source galaxy is computed, they are then used to lens the source galaxy catalog with its shapes and sizes and to apply the magnification to the magnitudes of each galaxy as described above.

¹¹ <https://bitbucket.org/gfcstanford/consistent-trees>

¹² <http://healpix.jpl.nasa.gov/>

The code is written in C, uses common software packages (GSL¹³, FFTW3¹⁴, FITS¹⁵, HDF5¹⁶) and is MPI-parallel so that it is quite portable and efficient. This code is publicly available for other researchers.¹⁷

For these simulations, we perform the ray tracing using an $n_{side} = 8192$ grid resulting in an effective pixel size of $\theta_{pix} = 0.46'$. The right panel of Fig. 3 shows measurements of $\xi_{+/-}$ without shape noise in three redshift bins averaged over the 18 Y1 footprints presented in this work compared to an analytic prediction for $\xi_{+/-}$ from HALOFIT (Takahashi et al. 2012). The bottom panel shows the fractional deviation of the simulations from the analytical predictions, with the grayed out regions demarcating scales below the pixel size used to do the raytracing. This resolution is sufficient for modeling $\xi_{+/-}$ at the scales used in the DES Y1 analysis, which are shown by the blue and green vertical lines. The dashed lines in the bottom panel show

$$\Delta\xi_{+/-}(\theta) = \frac{\xi_{+/-,\ell < \ell_{max}} - \xi_{+/-,\text{HALOFIT}}}{\xi_{+/-,\text{HALOFIT}}}$$

where

$$\xi_{+/-,\ell < \ell_{max}}(\theta) = \int \frac{d\ell \ell}{2\pi} \frac{J_{0/4}(\ell\theta)}{1 + \exp[\ln(\ell) - \ln(\ell_{max})]} \int d\chi \frac{q_{\kappa}^i(\chi) q_{\kappa}^j(\chi)}{\chi^2} P_{\text{HALOFIT}}\left(\frac{l+1/2}{\chi}, z(\chi)\right) \quad (\text{C2})$$

with

$$q_{\kappa}(\chi) = \frac{3H_0^2 \Omega_m}{2c^2} \frac{\chi}{a(\chi)} \int_{\chi}^{\chi_h} d\chi' \frac{n_{\kappa}(z(\chi')) dz/d\chi'}{\bar{n}_{\kappa}} \frac{\chi' - \chi}{\chi'} \quad (\text{C3})$$

i.e. $\xi_{+/-,\ell < \ell_{max}}(\theta)$ is the HALOFIT prediction but with the integral over ℓ truncated by an exponential function above a characteristic scale $\ell_{max} = \frac{\pi}{\theta_{pix}}$. This truncation is an approximation to the effect of resolution in the ray tracing algorithm, since the finite pixel size used to perform the raytracing calculations will manifest itself as an effect with a constant angular scale. The fact that the angular scale at which resolution effects begin diminishes as a function of redshift, instead of remaining constant, indicates that the resolution effects are sourced by effects in the underlying density field and not the raytracing itself. At low redshift, the fact that the deviation of the simulations from convergence matches the prediction using the truncation in ℓ as described above is likely a red herring produced by the fact that the physical scales that suffer from resolution effects in the lightcones translate to roughly the same angular scale at these redshifts as θ_{pix} .

Finally, once we have assigned magnitudes, shapes, and sizes to the galaxies, we lens the shapes using the relations

$$\varepsilon = \begin{cases} \frac{\varepsilon^{(s)+g}}{1+g^* \varepsilon} & |g| \leq 1, \\ \frac{1-g\varepsilon^{*(s)}}{\varepsilon^{*(s)+g^*}} & |g| > 1, \end{cases} \quad (\text{C4})$$

(Seitz & Schneider 1997) where the asterisk denotes complex conjugation, g is the complex reduced shear computed from the ray-tracing and the superscript (s) here and in the following denotes intrinsic source properties. The sizes and magnitudes are changed by gravitational lensing according to

$$r = \sqrt{|\mu|} r^{(s)}, \quad (\text{C5})$$

and

$$m = m^{(s)} - 2.5 \log(|\mu|), \quad (\text{C6})$$

where μ is the lensing magnification. Lensing deflections are also added to the true angular coordinates of each galaxy:

$$RA' = RA + \delta_{RA} \quad (\text{C7})$$

$$DEC' = DEC + \delta_{DEC} \quad (\text{C8})$$

where RA' and DEC' are the lensed coordinates and RA and DEC are the un-lensed coordinates.

¹³ <http://www.gnu.org/software/gsl>

¹⁴ <http://www.fftw.org>

¹⁵ <http://fits.gsfc.nasa.gov/iaufwg/iaufwg.html>

¹⁶ <http://www.hdfgroup.org/HDF5>

¹⁷ <https://github.com/beckermr/calclens>

D. DARK ENERGY SIMULATIONS WITH SECOND-ORDER LAGRANGIAN PERTURBATION THEORY INITIAL CONDITIONS

Although the catalog presented here uses a Λ CDM cosmology, In this work, we use second-order Lagrangian perturbation theory (2LPT) initial conditions (ICs) for our numerical simulations (see Section B). Our simulations implement changes to the background expansion rate (which subsequently changes the rate of growth of structure) at late times only and neglect any effects of dark energy perturbations. As pointed out by [Alimi et al. \(2010\)](#), this model is phenomenological rather than based on a single underlying theory. Previous works have used a rescaling of Λ CDM ICs (e.g., [Dolag et al. 2004](#)) or exact integrations of the first-order, linear growth equations for DE models with ZA ICs (e.g., [Alimi et al. 2010](#)). Here we present the ordinary differential equations (ODEs) for the first- and second-order growth factors along with prescriptions to integrate them for general DE models which change the background expansion rate only. These are the numerical coefficients needed for implementing 2LPT ICs with general DE models.

We start with equations E.18 and E.31 of Appendix E of [Jeong \(2010\)](#). These equations, when transformed to be functions of time t instead of the conformal variable $d\tau = dt/a$, are

$$\ddot{D}_1 + 2H(a)\dot{D}_1 - 4\pi G\rho_m(a)D_1 = 0 \quad (\text{D9})$$

$$\ddot{D}_2 + 2H(a)\dot{D}_2 - 4\pi G\rho_m(a)D_2 = -4\pi G\rho_m(a)D_1^2, \quad (\text{D10})$$

where $D_{1,2}$ are the first- and second-order growth factors, $H(a)$ is the Hubble function, a is the scale factor normalized to unity today, and $\rho_m(a) \propto a^3$ is the mean matter density. The dots denote derivatives with respect to time t . The most convenient form for numerical work is to apply an additional transformation to make them functions of the scale factor a . Additionally, it is convenient to express the mean matter density in units of the critical density so that $4\pi G\rho_m(a) = \frac{3}{2}H(a)^2\Omega_m(a)$. The final results are for D_1 ,

$$\frac{dD_1}{da} = D'_1 \quad (\text{D11})$$

$$\frac{dD'_1}{da} = \frac{3}{2} \frac{\Omega_m(a)}{a^2} D_1 - \left[\frac{3}{a} + \frac{d(H^2(a))}{da} \frac{1}{2H^2(a)} \right] D'_1, \quad (\text{D12})$$

and for D_2 ,

$$\frac{dD_2}{da} = D'_2 \quad (\text{D13})$$

$$\frac{dD'_2}{da} = \frac{3}{2} \frac{\Omega_m(a)}{a^2} D_2 - \left[\frac{3}{a} + \frac{d(H^2(a))}{da} \frac{1}{2H^2(a)} \right] D'_2 - \frac{3}{2} \frac{\Omega_m(a)}{a^2} D_1^2. \quad (\text{D14})$$

Here the primes denote the derivative of the growth factors. The second-order ODEs have been split into two first-order ODEs so that they can be integrated numerically. We use a high-order method from the publicly GNU Scientific Library¹⁸ to integrate these systems of ODEs.

To complete the integrations, one needs ICs for both $D_{1,2}$ and their derivatives. To do this, we follow [Komatsu et al. \(2009\)](#) and specify them in the matter dominated era where exact solutions are known and the simulations are started. These solutions are (e.g., [Bouchet et al. 1995](#))

$$D_1(a_i) = a_i \quad (\text{D15})$$

$$D'_1(a_i) = 1 \quad (\text{D16})$$

$$D_2(a_i) = -\frac{3}{7}a_i^2 \quad (\text{D17})$$

$$D'_2(a_i) = -\frac{6}{7}a_i. \quad (\text{D18})$$

¹⁸ <https://www.gnu.org/software/gsl/>

With these ICs, one obtains as the solution the strongest growing mode out of all of the homogenous and, for the second-order growth factor D_2 , homogeneous and particular solutions to the above equations. These modes are the appropriate solutions for initializing cosmological simulations.

Finally, one typically works with growth factors normalized to unity at the current epoch. For the linear order growth factor D_1 , one simply normalizes via $\tilde{D}_1(a) \rightarrow D_1(a)/D_1(a=1)$. Here $\tilde{D}_{1,2}$ denotes the normalized growth factors. For the second-order growth factor, this normalization corresponds to $\tilde{D}_2(a) \rightarrow D_2(a)/D_1^2(a=1)$. To see this, remember that $\tilde{D}_2(a)$ will be multiplied by a quantity which is $\propto \delta(k)^2$. Thus if $\delta(k)$ is normalized such that $P(k, a=1) = \frac{1}{(2\pi)^3 \delta(k+k')} \langle \delta(k)\delta(k') \rangle$ is the linear power spectrum today, then one must divide by $D_1^2(a=1)$ to obtain the proper normalization.

E. HIGH-REDSHIFT ADDGALS MODIFICATIONS

We use the ADDGALS algorithm, as described in Wechsler et al. (2019), to create a galaxy catalog. Here we summarize the extensions to this algorithm that are required to model higher redshift observables than discussed in Wechsler et al. (2019). ADDGALS is an empirical method for generating a catalog of galaxies to generate the distribution of galaxies and a minimal set of their photometric and spectroscopic properties. The algorithm matches the clustering properties predicted by SHAM, but without the use of high resolution halo merger histories. This is accomplished through a model fitting process to a SHAM catalog on our smaller, high resolution T1 simulation. This model is then used to populate our lower resolution lightcone simulations, L1, L2, L3, with galaxies with rest frame r -band absolute magnitudes, described in Section 3.3. A second step of the algorithm assigns SEDs to each galaxy allowing for the calculation of observed frame magnitudes as described in E.2.

E.1. Galaxy Luminosity Function

The main input that ADDGALS uses to generate galaxy populations is a rest frame r -band luminosity function as a function of redshift, $\phi(M_r, z)$. There are large systematic discrepancies between many luminosity function measurements due to differences in measuring photometry (Bernardi et al. 2012), correcting for incompleteness in flux (Blanton et al. 2005a) and sample variance of the small fields used at higher redshift (Loveday et al. 2015). Due to these issues, we focus on matching the cumulative number of observed counts as a function of apparent $griz$ magnitudes, $\bar{n}(> \bar{m})$ in DES Y1, a directly observable quantity. This quantity has limited constraining power on the luminosity function as a function of redshift, the quantity that ADDGALS requires as an input. Because of this, instead of constraining the full shape of $\phi(M_r, z)$ using $\bar{n}(> \bar{m})$, we start by taking the shape of the luminosity function as measured to high precision at low redshift from the work using the method described in Reddick et al. (2013) based on the SDSS spectroscopic sample and use the measurements of $\phi_*(z)$ from AGES (Cool et al. 2012) to account for redshift evolution. We then allow for additional freedom in $M_*(z)$, which we constrain using $\bar{n}(> \bar{m})$.

In particular, the functional form of the luminosity function that we use is a modified double-Schechter function with a Gaussian tail, as given by

$$\begin{aligned} \Phi(M, z) = & 0.4 \ln(10) e^{-10^{-0.4(M-M_*(z))}} \left(\phi_1(z) 10^{-0.4(M-M_*(z))(\alpha_1+1)} + \phi_2(z) 10^{-0.4(M-M_*(z))(\alpha_2+1)} \right) \\ & + \frac{\phi_3(z)}{\sqrt{2\pi\sigma_{hi}^2}} e^{\frac{-(M-M_{hi}(z))^2}{2\sigma_{hi}^2}}. \end{aligned} \quad (\text{E19})$$

where

$$M_{*/hi}(z) = M_{*/hi,0} + Q \left(\frac{1}{1+z} - \frac{1}{1.1} \right) \quad (\text{E20})$$

and

$$\phi_i(z) = \phi_{i,0} + Pz \quad (\text{E21})$$

We first produce a catalog of galaxies with the luminosity function model as described above with the values for Q and P taken from Cool et al. (2012), where the same values for Q and P are used for M_* and M_{hi} and all the ϕ_i respectively. The double Schechter function is motivated by evidence that the faint end of the luminosity function deviates from a single power law (Blanton et al. 2003, e.g.). The Gaussian is intended to model observed deviations from the exponential fall off prescribed by a Schechter function at the bright end (Reddick et al. 2013; Bernardi et al. 2012, e.g.).

We then parameterize the discrepancy between our luminosity function model and the luminosity function of DES galaxies as a simple shift in M_* as a function of z

$$\Delta M_*(z) = \frac{\Delta Q}{1.1} \frac{0.1-z}{1+z} \quad (\text{E22})$$

and fit for ΔQ by maximizing the log likelihood given by

$$\log \mathcal{L} \propto [\bar{n}^{DES} - \bar{n}(\Delta Q)] \Sigma^{-1} [\bar{n}^{DES} - \bar{n}(\Delta Q)]^T \quad (\text{E23})$$

where \bar{n}^{DES} is the cumulative number of galaxies as a function of magnitude per square degree measured in the DES overlap with COSMOS (which is approximately 1 magnitude deeper than the DES Y1 wide field). $\bar{n}(\Delta Q)$ is the cumulative number of galaxies per square degree in Buzzard when applying a shift to each galaxy's *griz* magnitudes given by $\Delta M_*(z)$. Σ is approximated as diagonal and estimated as the Poisson error on \bar{n}^{DES} and $\bar{n}(\Delta Q)$ added in quadrature. Magnitudes ranging from $\{18.6, 17.8, 17.4, 17.1\}$ down to magnitudes $\{24.38, 24.25, 23.71, 23.26\}$ in *g*, *r*, *i*, and *z*-band respectively are used in the fits. The bright end of this cut is imposed to mitigate the large amount of sample variance in the ~ 1.5 square degree COSMOS field. At the faint end, there should be $> 10\%$ contributions from galaxies with $z > 2.3$, which are not able to be placed in our simulations.

E.2. Galaxy SEDs and Multi-band Photometry

We map galaxy SEDs from the data onto our simulated galaxies by using the relation between M_r , projected galaxy density, and SED as measured from SDSS. Using a set of spectroscopic galaxies comprising 570,000 objects from the SDSS VAGC (Blanton et al. 2005b) with $0.005 < z < 0.2$, we measure Σ_5 , the projected distance to the 5th nearest galaxy brighter than $M_r = -19.75$ in redshift slices with $\Delta z = 0.02$. Similar quantities have been shown to correlate strongly with star formation rate (Cooper et al. 2006). In bins of M_r and z we then rank each galaxy by this density, yielding the rank \mathcal{R}_{Σ_5} . By using \mathcal{R}_{Σ_5} instead of Σ_5 , we avoid issues related to evolving number densities that we would otherwise encounter due to our use of a magnitude limited, as opposed to volume limited, sample for our training set.

Identical measurements are made for our simulated galaxies and for each simulated galaxy, g_i , with absolute magnitude $M_{r,i}$, redshift z_i and density rank $\mathcal{R}_{\Sigma_5,i}$ we identify a set of possible matches in the data, $\{g_{j,\text{SDSS}}\}$, by selecting galaxies in the data in the same $M_r - \mathcal{R}_{\Sigma_5}$ bin. If we were modeling the same redshift range as our training set, we could sample uniformly from this set to draw an SED for g_i . This is not the case in this work, as we wish to model a much larger redshift range than the training set we are using. Thus we must account for redshift evolution of the $M_r - \mathcal{R}_{\Sigma_5} - \text{SED}$ relationship. We do this by assuming that our training set spans the set of SEDs that may appear in DES, but allow for the possibility that the distribution of these SEDs evolves as a function of redshift and absolute magnitude. To model this evolution, we define the quantity $\mathcal{W}_{\text{red}}(M_r, z)$, as ratio of the red fraction of galaxies at redshift z relative to the low redshift red fraction (at $z < 0.2$). A galaxy is deemed to be on the red sequence if it satisfies

$$^{0.1}(g-r) > 0.15 - 0.03^{0.1} M_r. \quad (\text{E24})$$

We then define

$$\mathcal{W}_{\text{red}}(M_r, z) = \frac{P(\text{red}|z, M_r; \text{PRIMUS})}{P(\text{red}|0.0 < z < 0.2, M_r; \text{PRIMUS})}, \quad (\text{E25})$$

i.e. the ratio of the red fraction as a function of *r*-band absolute magnitude in PRIMUS (Coil et al. 2011), to that found at low redshift in PRIMUS. We then choose a galaxy from the set of matches with SDSS, $\{g_{j,\text{SDSS}}\}$, choosing a red galaxy with probability given by

$$P(\text{red}|M_r, z, \mathcal{R}_{\Sigma_5}) = P(\text{red}|M_r, z, \mathcal{R}_{\Sigma_5}; \text{SDSS}) \mathcal{W}_{\text{red}}(M_r, z) \quad (\text{E26})$$

and assign its SED to g_i using KCORRECT coefficients. KCORRECT is a SED template fitting method described in Blanton & Roweis (2007) that represents SEDs as a linear combination of 5 templates which were tuned to match SDSS *griz* photometry. Using this SED representation, we are then able to generate multiband photometry for each galaxy.

E.3. Adding Realistic Galaxy Shapes and Sizes

Gravitational lensing changes the shape, size, and position of galaxy images. To include the effects on size and shape in our simulations we first need a model for the intrinsic distributions of these quantities before the effects of lensing are applied to them. We are primarily interested in modeling weak gravitational lensing, and we limit the shape model to ellipticities and neglect higher order terms describing more complex galaxy shapes.

In real imaging data a distinction has to be made between an object's ellipticity and the shear estimated from its observed ellipticity. Shear estimation methods call this e.g. the shear polarizability (Kaiser et al. 1995, KSB). For purely catalog based simulations such a distinction is not necessary and we base our model for the intrinsic ellipticity of objects on the shear estimators reported by the Zuntz et al. (2018) implementation of the METACALIBRATION algorithm. We also wish to model galaxy angular sizes, by re-sampling the SExtractor (Bertin & Arnouts 1996) measurements of FLUX_RADIUS in the same DES Y1 data set. The distribution function of these shear estimators, which we use as intrinsic ellipticity distribution, and sizes, is described by an Gaussian mixture model. In particular we fit a Gaussian mixture with 20 components to the joint distribution of absolute ellipticity, FLUX_RADIUS, and i -band magnitude in the DES Y1 METACALIBRATION sample, deconvolving magnitude errors using the method described in Bovy et al. (2010).

$$p(|\varepsilon|, r, m_i) = \sum_{i=0}^{19} \alpha_i \mathcal{N}(\mu_i, \Sigma_i) \quad (\text{E27})$$

Here $|\varepsilon|$ is the absolute value of the ellipticity, r is the FLUX_RADIUS, μ_i and Σ_i are each Gaussian components' mean and covariance matrix, and α_i are the component weights, which sum to unity. Ellipticities and sizes are then drawn for each galaxy by conditioning E27 on the galaxies i -band magnitude and sampling from the resulting conditional distribution.

E.4. Photometric errors

Once the catalogs have been lensed and are rotated into the DES Y1 footprint, we apply a straightforward model to include photometric errors. Photometric errors provide a significant source of contamination, particularly for apparently faint galaxies. These errors will cause both objects above the detection threshold to scatter out of our detection limits, as well as causing many more dim objects to scatter in. Modeling these errors appropriately can thus be important for a number of analyses.

To match the DES Y1 magnitude and magnitude error distribution we use the map of $10\text{-}\sigma$ limiting magnitudes determined from the DES Y1 Multi-Object Fitting (MOF) photometry in $griz$ as well as the effective exposure time (t_{eff}) of the survey in each band. In this way we realistically incorporate depth variations from the Y1 footprint in our simulations, neglecting the dependence of detection efficiency on galaxy size. Our model for photometric errors using these ingredients is as follows.

We use a straightforward method of calculating the Poisson noise for the flux of a simulated galaxy plus the sky noise in a particular band. Here, the total signal from these two sources (galaxy and sky) are given by the relation:

$$\begin{aligned} S_{\text{gal}} &= 10^{-0.4(m_{\text{gal}} - ZP)} \times t_{\text{eff}} \\ S_{\text{sky}} &= f_{\text{sky}} \times t_{\text{eff}}, \end{aligned} \quad (\text{E28})$$

where m_{gal} is the magnitude of a galaxy and f_{sky} is the sky noise (in a particular band), and t_{eff} is the effective exposure time in nominal observing conditions as defined in Drlica-Wagner et al. (2018). In all cases we set the zero-point $ZP = 22.5$, and all fluxes in the data tables are converted to nanomaggies such that:

$$m = 22.5 - 2.5 \log_{10} f_{\text{nmgy}}. \quad (\text{E29})$$

Finally, we note that the sky noise parameter, f_{sky} , can be estimated from the 10σ limiting magnitude m_{lim} and the associated f_{lim} :

$$f_{\text{sky}} = \frac{f_{\text{lim},1}^2 \times t_{\text{eff}}}{100} - f_{\text{lim},1}, \quad (\text{E30})$$

where $f_{\text{lim},1}$ is the 1 second flux at the limiting magnitude given by Eqn. E28. Given the galaxy flux and sky flux, the typical noise associated with each galaxy will be given by a random draw from a distribution of width $\sigma_{\text{flux}} = \sqrt{S_{\text{gal}} + S_{\text{sky}}}$. Then, for

each galaxy, we convert the total observed flux and error to nanomaggies, such that $f_{\text{nmgy}} = S_{\text{gal,obs}}/t_{\text{eff}}$. Finally, we calculate the magnitude and error:

$$\begin{aligned} m_{\text{obs}} &= 22.5 - 2.5 \log_{10}(f_{\text{nmgy}}) \\ m_{\text{err,obs}} &= \frac{2.5}{\ln(10)} \frac{f_{\text{err,nmgy}}}{f_{\text{nmgy}}} \end{aligned} \quad (\text{E31})$$

Note that, as is possible with observational data, this results in a number of dim galaxies having negative fluxes in one or more bands in cases with large photometric errors. These are set to 99 in the magnitude table.

F. DIFFERENCES FROM PREVIOUS CATALOG VERSIONS

Previous versions of these catalogs contained a large bias in the mean redshift of the fourth source bin that was significantly ruled out by the data (MacCrann et al. 2018). The selection used for those source catalogs was

1. Mask all regions of the footprint where limiting magnitudes and PSF sizes cannot be estimated.
2. $m_r < -2.5 \log_{10}(1.5) + m_{r,\text{lim}}$
3. $\sqrt{r_{\text{gal}}^2 + (0.5 r_{\text{PSF}})^2} > 0.75 r_{\text{PSF}}$
4. $m_r < 22.07 + 1.08 z$

The source of this bias is our use templates constrained by SDSS when incorporating colors in our simulations. These templates are constrained by SDSS *griz* photometry at $z \leq 0.2$. Because of this, the rest frame UV portions of the templates are relatively unconstrained, and it is this portion of our spectra which appear in the DES band-passes at $z > \sim 1.5$, leading to little evolution in color of our galaxies above this redshift. As such, BPZ cannot distinguish between galaxies at $z = 1.5$ and higher redshifts, leading to many higher redshift galaxies contaminating the highest redshift source redshift bin ($0.9 < z_{\text{BPZ}} \leq 1.3$). The previous version of these catalogs, BUZZARD v1.6 had significantly more bright high redshift galaxies than the current version, exacerbating the problem with high redshift colors. High redshift SEDs in our simulations represent one of the major outstanding deficiencies of these simulations, and we are actively pursuing upgrades which will improve this performance. Until then, high-redshift galaxy colors in these simulations should be used with caution.

REFERENCES

- Abazajian, K. N., Adshead, P., Ahmed, Z., et al. 2016, arXiv e-prints, arXiv:1610.02743
- Alimi, J. M., Füzfa, A., Boucher, V., et al. 2010, *MNRAS*, **401**, 775
- Arkani-Hamed, N., & Maldacena, J. 2015, ArXiv e-prints, arXiv:1503.08043
- Becker, M. R. 2013, *MNRAS*, **435**, 115
- Becker, M. R., McKay, T. A., Koester, B., et al. 2007, *APJ*, **669**, 905
- Becker, M. R., Troxel, M. A., MacCrann, N., et al. 2016, *PhRvD*, **94**, 022002
- Behroozi, P., Wechsler, R., Hearin, A., & Conroy, C. 2018, ArXiv e-prints, arXiv:1806.07893
- Behroozi, P. S., Wechsler, R. H., & Wu, H.-Y. 2013a, *APJ*, **762**, 109
- Behroozi, P. S., Wechsler, R. H., Wu, H.-Y., et al. 2013b, *APJ*, **763**, 18
- Benítez, N. 2000, *APJ*, **536**, 571
- Benson, A. J., Lacey, C. G., Baugh, C. M., Cole, S., & Frenk, C. S. 2002, *MNRAS*, **333**, 156
- Berlind, A. A., & Weinberg, D. H. 2002, *ApJ*, **575**, 587
- Bernardi, M., Meert, A., Vikram, V., et al. 2012, ArXiv e-prints, arXiv:1211.6122
- Bertin, E., & Arnouts, S. 1996, *Astronomy and Astrophysics Supplement Series*, **117**, 393
- Blanton, M. R., Lupton, R. H., Schlegel, D. J., et al. 2005a, *APJ*, **631**, 208
- Blanton, M. R., & Roweis, S. 2007, *AJ*, **133**, 734
- Blanton, M. R., Hogg, D. W., Bahcall, N. A., et al. 2003, *APJ*, **592**, 819
- Blanton, M. R., Schlegel, D. J., Strauss, M. A., et al. 2005b, *AJ*, **129**, 2562
- Bleem, L. E., Stalder, B., de Haan, T., et al. 2015, *The Astrophysical Journal Supplement Series*, **216**, 27
- Bonnett, C., Troxel, M. A., Hartley, W., et al. 2016, *PhRvD*, **94**, 042005

- Bouchet, F. R., Colombi, S., Hivon, E., & Juszkiewicz, R. 1995, *A&A*, 296, 575
- Bovy, J., Hogg, D. W., & Roweis, S. T. 2010, *Extreme Deconvolution: Density Estimation using Gaussian Mixtures in the Presence of Noisy, Heterogeneous and Incomplete Data*, Astrophysics Source Code Library
- Bower, R. G., Benson, A. J., Malbon, R., et al. 2006, *MNRAS*, 370, 645
- Bryan, G. L., & Norman, M. L. 1998, *APJ*, 495, 80
- Carretero, J., Castander, F. J., Gaztañaga, E., Croce, M., & Fosalba, P. 2015, *MNRAS*, 447, 646
- Chang, C., Pujol, A., Mawdsley, B., et al. 2018, *MNRAS*, 475, 3165
- Coil, A. L., Blanton, M. R., Burles, S. M., et al. 2011, *APJ*, 741, 8
- Cole, S., Lacey, C. G., Baugh, C. M., & Frenk, C. S. 2000, *MNRAS*, 319, 168
- Conroy, C., Wechsler, R. H., & Kravtsov, A. V. 2006a, *APJ*, 647, 201
- . 2006b, *APJ*, 647, 201
- Cool, R. J., Eisenstein, D. J., Kochanek, C. S., et al. 2012, *APJ*, 748, 10
- Cooper, M. C., Newman, J. A., Croton, D. J., et al. 2006, *MNRAS*, 370, 198
- Costanzi, M., Rozo, E., Rykoff, E. S., et al. 2019, *MNRAS*, 482, 490
- Crocce, M., Castander, F. J., Gaztañaga, E., Fosalba, P., & Carretero, J. 2015, *MNRAS*, 453, 1513
- Crocce, M., Pueblas, S., & Scoccimarro, R. 2006, *MNRAS*, 373, 369
- Cunha, C. E., Huterer, D., Busha, M. T., & Wechsler, R. H. 2012, *MNRAS*, 423, 909
- Cunha, C. E., Huterer, D., Lin, H., Busha, M. T., & Wechsler, R. H. 2014, *MNRAS*, 444, 129
- Davis, C., Gatti, M., Vielzeuf, P., et al. 2017, ArXiv e-prints, arXiv:1710.02517
- DES Collaboration, Abbott, T. M. C., Abdalla, F. B., et al. 2017, ArXiv e-prints, arXiv:1708.01530
- Dolag, K., Bartelmann, M., Perrotta, F., et al. 2004, *A&A*, 416, 853
- Dong, F., Pierpaoli, E., Gunn, J. E., & Wechsler, R. H. 2008, *APJ*, 676, 868
- Drlica-Wagner, A., Sevilla-Noarbe, I., Rykoff, E. S., et al. 2018, *The Astrophysical Journal Supplement Series*, 235, 33
- Evrard, A. E. 1988, *MNRAS*, 235, 911
- Evrard, A. E., MacFarland, T. J., Couchman, H. M. P., et al. 2002, *APJ*, 573, 7
- Fosalba, P., Crocce, M., Gaztañaga, E., & Castander, F. J. 2015a, *MNRAS*, 448, 2987
- Fosalba, P., Gaztañaga, E., Castander, F. J., & Crocce, M. 2015b, *MNRAS*, 447, 1319
- Fosalba, P., Gaztañaga, E., Castander, F. J., & Manera, M. 2008, *MNRAS*, 391, 435
- Friedrich, O., Gruen, D., DeRose, J., et al. 2018, *PhRvD*, 98, 023508
- Gatti, M., Vielzeuf, P., Davis, C., et al. 2018, *MNRAS*, 477, 1664
- Gerdes, D. W., Sypniewski, A. J., McKay, T. A., et al. 2010, *APJ*, 715, 823
- Górski, K. M., Hivon, E., Banday, A. J., et al. 2005, *APJ*, 622, 759
- Gruen, D., Friedrich, O., Krause, E., et al. 2018, *PhRvD*, 98, 023507
- Guo, Q., White, S., Angulo, R. E., et al. 2013, *MNRAS*, 428, 1351
- Hansen, S. M., Sheldon, E. S., Wechsler, R. H., & Koester, B. P. 2009, *APJ*, 699, 1333
- Hao, J., McKay, T. A., Koester, B. P., et al. 2010, *APJs*, 191, 254
- Harnois-Déraps, J., Amon, A., Choi, A., et al. 2018, *MNRAS*, 481, 1337
- Hearin, A. P., & Watson, D. F. 2013, *MNRAS*, 435, 1313
- Hilbert, S., Hartlap, J., White, S. D. M., & Schneider, P. 2009, *A&A*, 499, 31
- Hopkins, P. F., Wetzel, A., Kereš, D., et al. 2018, *MNRAS*, 480, 800
- Hoyle, B., Gruen, D., Bernstein, G. M., et al. 2018, *MNRAS*, 478, 592
- Huff, E., & Mandelbaum, R. 2017, arXiv e-prints, arXiv:1702.02600
- Izard, A., Fosalba, P., & Crocce, M. 2018, *MNRAS*, 473, 3051
- Jain, B., Seljak, U., & White, S. 2000, *APJ*, 530, 547
- Jeong, D. 2010, PhD thesis, University of Texas at Austin
- Jing, Y. P. 1998, *ApJ*, 503, L9
- Johnston, D. E., Sheldon, E. S., Wechsler, R. H., et al. 2007, ArXiv e-prints, arXiv:0709.1159
- Kaiser, N., Squires, G., & Broadhurst, T. 1995, *APJ*, 449, 460
- Kauffmann, G., White, S. D. M., & Guiderdoni, B. 1993, *MNRAS*, 264, 201
- Kim, J.-h., Abel, T., Agertz, O., et al. 2014, *The Astrophysical Journal Supplement Series*, 210, 14
- Knebe, A., Knollmann, S. R., Muldrew, S. I., et al. 2011, *MNRAS*, 415, 2293
- Koester, B. P., McKay, T. A., Annis, J., et al. 2007a, *APJ*, 660, 239
- . 2007b, *APJ*, 660, 221
- Komatsu, E., Dunkley, J., Nolte, M. R., et al. 2009, *The Astrophysical Journal Supplement Series*, 180, 330
- Krause, E., Eifler, T. F., Zuntz, J., et al. 2017, ArXiv e-prints, arXiv:1706.09359
- Laigle, C., McCracken, H. J., Ilbert, O., et al. 2016, *The Astrophysical Journal Supplement Series*, 224, 24
- Lawrence, E., Heitmann, K., Kwan, J., et al. 2017, *APJ*, 847, 50
- Lehmann, B. V., Mao, Y.-Y., Becker, M. R., Skillman, S. W., & Wechsler, R. H. 2017, *APJ*, 834, 37

- Leistedt, B., Peiris, H. V., Elsner, F., et al. 2016, *The Astrophysical Journal Supplement Series*, 226, 24
- Limber, D. N. 1954, *APJ*, 119, 655
- Loveday, J., Norberg, P., Baldry, I. K., et al. 2015, *MNRAS*, 451, 1540
- MacCrann, N., DeRose, J., Wechsler, R. H., et al. 2018, *MNRAS*, 480, 4614
- Mandelbaum, R., Seljak, U., Kauffmann, G., Hirata, C. M., & Brinkmann, J. 2006, *MNRAS*, 368, 715
- Mao, Y.-Y., Kovacs, E., Heitmann, K., et al. 2018, *The Astrophysical Journal Supplement Series*, 234, 36
- Marinacci, F., Vogelsberger, M., Pakmor, R., et al. 2018, *MNRAS*, 480, 5113
- McClintock, T., Rozo, E., Becker, M. R., et al. 2018, ArXiv e-prints, arXiv:1804.05866
- Miller, C. J., Nichol, R. C., Reichart, D., et al. 2005, *AJ*, 130, 968
- Moster, B. P., Naab, T., & White, S. D. M. 2018, *MNRAS*, 477, 1822
- Naiman, J. P., Pillepich, A., Springel, V., et al. 2018, *MNRAS*, 477, 1206
- Nelson, D., Pillepich, A., Springel, V., et al. 2018, *MNRAS*, 475, 624
- Perlmutter, S., Aldering, G., Goldhaber, G., et al. 1999, *APJ*, 517, 565
- Pillepich, A., Nelson, D., Hernquist, L., et al. 2018, *MNRAS*, 475, 648
- Planck Collaboration, Aghanim, N., Akrami, Y., et al. 2018, ArXiv e-prints, arXiv:1807.06209
- Reddick, R. M., Wechsler, R. H., Tinker, J. L., & Behroozi, P. S. 2013, *APJ*, 771, 30
- Riess, A. G., Filippenko, A. V., Challis, P., et al. 1998, *AJ*, 116, 1009
- Rozo, E., Wechsler, R. H., Koester, B. P., Evrard, A. E., & McKay, T. A. 2007a, ArXiv e-prints, astro
- Rozo, E., Wechsler, R. H., Koester, B. P., et al. 2007b, ArXiv e-prints, astro
- Rozo, E., Rykoff, E. S., Abate, A., et al. 2016, *MNRAS*, 461, 1431
- Rubin, V. C., Ford, W. K., J., & Thonnard, N. 1980, *APJ*, 238, 471
- Rykoff, E. S., Rozo, E., Busha, M. T., et al. 2014, *APJ*, 785, 104
- Schaye, J., Crain, R. A., Bower, R. G., et al. 2015, *MNRAS*, 446, 521
- Schneider, P., Ehlers, J., & Falco, E. E. 1992, *Gravitational Lenses*
- Seitz, C., & Schneider, P. 1997, *A&A*, 318, 687
- Seljak, U. 2000, *MNRAS*, 318, 203
- Sheldon, E. S., & Huff, E. M. 2017, *ApJ*, 841, 24
- Sheldon, E. S., Johnston, D. E., Masjedi, M., et al. 2009, *APJ*, 703, 2232
- Soares-Santos, M., de Carvalho, R. R., Annis, J., et al. 2011, *APJ*, 727, 45
- Somerville, R. S., & Primack, J. R. 1999, *MNRAS*, 310, 1087
- Springel, V. 2005, *MNRAS*, 364, 1105
- Springel, V., Pakmor, R., Pillepich, A., et al. 2018, *MNRAS*, 475, 676
- Takahashi, R., Hamana, T., Shirasaki, M., et al. 2017, *APJ*, 850, 24
- Takahashi, R., Sato, M., Nishimichi, T., Taruya, A., & Oguri, M. 2012, *APJ*, 761, 152
- Tasitsiomi, A., Kravtsov, A. V., Wechsler, R. H., & Primack, J. R. 2004, *APJ*, 614, 533
- Tassev, S., Zaldarriaga, M., & Eisenstein, D. J. 2013, *Journal of Cosmology and Astro-Particle Physics*, 2013, 036
- Tinker, J., Wetzel, A., & Conroy, C. 2011, ArXiv e-prints, arXiv:1107.5046
- Tinker, J. L., Robertson, B. E., Kravtsov, A. V., et al. 2010, *APJ*, 724, 878
- Troxel, M. A., MacCrann, N., Zuntz, J., et al. 2018, *PhRvD*, 98, 043528
- van den Bosch, F. C., Yang, X., Mo, H. J., et al. 2007, *MNRAS*, 376, 841
- Wechsler, R. H., DeRose, J. D., Busha, M. T., Becker, M. R., et al. 2019, to be submitted
- Wechsler, R. H., & Tinker, J. L. 2018, *Annual Review of Astronomy and Astrophysics*, 56, 435
- Weinberg, D. H., Mortonson, M. J., Eisenstein, D. J., et al. 2013, *PhR*, 530, 87
- White, S. D. M., & Frenk, C. S. 1991, *ApJ*, 379, 52
- Yang, X., Mo, H. J., & van den Bosch, F. C. 2003, *MNRAS*, 339, 1057
- Zehavi, I., Zheng, Z., Weinberg, D. H., et al. 2011, *ApJ*, 736, 59
- Zheng, Z., Berlind, A. A., Weinberg, D. H., et al. 2005, *ApJ*, 633, 791
- Zu, Y., & Mandelbaum, R. 2015, *MNRAS*, 454, 1161
- Zuntz, J., Sheldon, E., Samuroff, S., et al. 2018, *MNRAS*, 481, 1149
- Zwicky, F. 1933, *Helvetica Physica Acta*, 6, 110